

Correlating the CDF W -mass shift with the muon $g - 2$ and the $b \rightarrow s\ell^+\ell^-$ transitions

Xin-Qiang Li,^{a,b} Ze-Jun Xie,^a Ya-Dong Yang^{a,c} and Xing-Bo Yuan^a

^a*Institute of Particle Physics and Key Laboratory of Quark and Lepton Physics (MOE),
Central China Normal University, Wuhan, Hubei 430079, China*

^b*Center for High Energy Physics, Peking University, Beijing 100871, China*

^c*Institute of Particle and Nuclear Physics, Henan Normal University, Xinxiang 453007, China*

E-mail: xqli@mail.ccnu.edu.cn, xiezejun@mails.ccnu.edu.cn,
yangyd@ccnu.edu.cn, y@ccnu.edu.cn

ABSTRACT: Motivated by the latest CDF W -mass measurement as well as the muon $g - 2$ anomaly and the discrepancies observed in $b \rightarrow s\ell^+\ell^-$ transitions, we propose an extension of the Standard Model (SM) with the $SU(2)_L$ -singlet vector-like fermion partners that are featured by additional $U(1)'$ gauge symmetry. The fermion partners have the same SM quantum numbers as of the right-handed SM fermions, and can therefore mix with the latter after the electroweak and the $U(1)'$ symmetry breaking. As a result, desirable loop-level corrections to the $(g - 2)_\mu$, the W -boson mass m_W and the Wilson coefficient \mathcal{C}_9 in $b \rightarrow s\mu^+\mu^-$ transitions can be obtained. The final allowed parameter space is also consistent with the constraints from the $Z \rightarrow \mu^+\mu^-$ decay, the neutrino trident production and the LHC direct searches for the vector-like quarks and leptons.

Contents

1	Introduction	1
2	Model	2
2.1	Quark sector	3
2.2	Lepton sector	5
2.3	Choice of the model parameters	6
3	Theoretical framework	7
3.1	W -mass shift and oblique parameters	7
3.2	$b \rightarrow s\ell^+\ell^-$ transitions	9
3.3	Muon $g - 2$	10
3.4	Neutrino trident production	11
3.5	$Z\mu\mu$ and $W\mu\nu$ couplings	11
4	Numerical analysis	12
4.1	$Z\mu\mu$ and $W\mu\nu$ couplings	13
4.2	W -boson mass and global EW fit	14
4.3	Muon $g - 2$ and neutrino trident production	15
4.4	$b \rightarrow s\ell^+\ell^-$ processes	17
4.5	Collider phenomenology	19
5	Conclusion	22
A	One-loop corrections to $Z \rightarrow \ell^+\ell^-$	22
B	Global fit of $b \rightarrow s\ell^+\ell^-$ transitions	24
C	Loop functions	24

1 Introduction

The Standard Model (SM) of particle physics has proven incredibly successful in describing most phenomena observed in experiments [1]. At present, the major focus of the Large Hadron Colliders (LHC) is the direct searches for new particles and new interactions beyond the SM. While no confirmed direct signals for new physics (NP) beyond the SM have been observed at the LHC so far, several interesting hints of NP have been emerging from the precision measurements.

The long-standing anomaly of the muon $g - 2$ provides an intriguing hint of NP. The latest measurement by the Muon $g - 2$ collaboration at Fermilab [2], after combined with the previous measurement by the Brookhaven E821 experiment [3], shows a 4.2σ discrepancy with the SM prediction [4]:

$$\Delta a_\mu = a_\mu^{\text{exp}} - a_\mu^{\text{SM}} = (251 \pm 59) \times 10^{-11}, \quad (1.1)$$

with $a_\mu = (g - 2)_\mu/2$. On the theoretical side, further detailed studies are presently on going to improve the precision of the hadronic contribution to the muon $g - 2$ [5–9] (see also ref. [10] for a recent review).

Another interesting hint of NP comes from the updated measurement of the W -boson mass by the Collider Detector at Fermilab (CDF) collaboration [11]. Using the complete dataset collected by the CDF II detector, the CDF collaboration reported a value [11]

$$m_W^{\text{CDF}} = 80.4335 \pm 0.0064_{\text{stat}} \pm 0.0069_{\text{syst}} \text{ GeV}. \quad (1.2)$$

Such a high precision measurement deviates from the average of the previous measurements from LEP, CDF, D0 and ATLAS, $m_W^{\text{PDG}} = 80.379 \pm 0.012 \text{ GeV}$ [1], as well as from the LHCb measurement $m_W^{\text{LHCb}} = 80.354 \pm 0.031 \text{ GeV}$ [12], and the recent ATLAS measurement $m_W^{\text{ATLAS}} = 80.360 \pm 0.016 \text{ GeV}$ [13]. Furthermore, it shows a 7σ deviation from the SM expectation obtained through a global electroweak (EW) fit, $m_W^{\text{SM}} = 80.357 \pm 0.006 \text{ GeV}$ [1]. If confirmed by future precision measurements, this anomaly could imply another sign of NP beyond the SM.

Finally, several interesting discrepancies with the SM predictions have been observed in the $b \rightarrow s\ell^+\ell^-$ (with $\ell = e, \mu$) processes over the last decade. Notably, the experimental picture has changed dramatically at the end of 2022: the previous $R_{K^{(*)}}$ anomalies were not confirmed by the updated LHCb measurements [14, 15], and the recent CMS measurement of the branching fraction $\mathcal{B}(B_s \rightarrow \mu^+\mu^-)$ [16] made the current world average [17] in excellent agreement with the SM prediction [18, 19]. However, several observables in the $b \rightarrow s\ell^+\ell^-$ transitions, especially the angular observable P'_5 in $B \rightarrow K^*\mu^+\mu^-$ [20] as well as the branching ratios of $B \rightarrow K^{(*)}\mu^+\mu^-$ [21] and $B_s \rightarrow \phi\mu^+\mu^-$ [22], still show $2 \sim 3\sigma$ deviations from the corresponding SM predictions. Furthermore, the recent global fits show that the overall consistency of the current $b \rightarrow s\ell^+\ell^-$ data with the theoretical predictions can be significantly improved by adding NP to the short-distance Wilson coefficient \mathcal{C}_9 [23–27].

It is noted that, within the SM, the $(g - 2)_\mu$, the W -boson mass and the $b \rightarrow s\ell^+\ell^-$ transition all receive significant contributions from the loop diagrams with quarks or leptons. These loop diagrams could also be mediated by the NP fermions that have the same SM quantum numbers as of the SM ones. Therefore, these NP effects could simultaneously explain the data mentioned above. In this paper, in order to investigate such a possibility, we construct a NP model in which the SM is extended with the vector-like fermion partners that are featured by additional $U(1)'$ gauge symmetry. We assume that the fermion partners are $SU(2)_L$ singlets and have the same SM quantum numbers as of the right-handed SM fermions. After the EW and the $U(1)'$ symmetry are spontaneously broken, possible mixings between the fermion partners and the SM right-handed fermions are obtained, which can result in desirable loop-level corrections to the $(g - 2)_\mu$, m_W , and \mathcal{C}_9 . Our model can be regarded as an extension of the one introduced in refs. [28, 29]. We will also consider the various constraints coming from the $Z \rightarrow \mu^+\mu^-$ decay, the neutrino trident production and the LHC direct searches for the vector-like quarks and leptons.

The paper is organized as follows: In section 2, we introduce the NP model based on a new $U(1)'$ symmetry. In section 3, we recapitulate the theoretical framework for the various processes and investigate the NP effects on them. Our detailed numerical results and discussions are presented in section 4. We conclude in section 5. Details of the one-loop corrections to the $Z\mu\mu$ coupling and the global fit of the $b \rightarrow s\ell^+\ell^-$ processes are presented in appendices A and B, respectively. The relevant loop functions are collected in appendix C.

2 Model

As discussed in ref. [28], in order to simultaneously accommodate the m_W^{CDF} , the $(g - 2)_\mu$ anomaly and the $b \rightarrow s\ell^+\ell^-$ discrepancies, one can introduce the new fermions that are characterized by

	SM							NP				
	Q_{3L}	u_{3R}	L_{2L}	L_{3L}	e_{2R}	e_{3R}	H	$U'_{L/R}$	$E_{L/R}$	Φ_ℓ	Φ_t	ϕ
$SU(3)_C$	3	3	1	1	1	1	1	3	1	1	1	1
$SU(2)_L$	2	1	2	2	1	1	2	1	1	1	1	1
$U(1)_Y$	1/6	2/3	-1/2	-1/2	-1	-1	1/2	2/3	-1	0	0	0
$U(1)'$	0	0	q_ℓ	$-q_\ell$	q_ℓ	$-q_\ell$	0	q_t	0	$-q_\ell$	q_t	0

Table 1: Quantum numbers of the SM and NP fields in our model under the $SU(3)_C \otimes SU(2)_L \otimes U(1)_Y \otimes U(1)'$ gauge symmetry. See text for more details.

additional $U(1)'$ gauge symmetry and have the same SM quantum numbers as of the SM ones. To this end, let us firstly introduce our model based on the new $U(1)'$ symmetry, where the SM and NP fields as well as their charges under the $SU(3)_C \otimes SU(2)_L \otimes U(1)_Y \otimes U(1)'$ gauge symmetry are given in table 1.

2.1 Quark sector

The quark sector of the model is identical to that introduced in refs. [28, 29]. All the SM quarks do not carry the $U(1)'$ charge, while a vector-like top partner with

$$U'_{L/R} = (\mathbf{3}, \mathbf{1}, 2/3, q_t), \quad (2.1)$$

and a complex scalar with

$$\Phi_t = (\mathbf{1}, \mathbf{1}, 0, q_t), \quad (2.2)$$

are introduced, where the quantum numbers in brackets dictate the transformations under the $SU(3)_C \otimes SU(2)_L \otimes U(1)_Y \otimes U(1)'$ gauge symmetry.

The general Lagrangian involving the top partner $U'_{L/R}$, the SM Higgs doublet H and the scalar Φ_t can be written as

$$\mathcal{L} \supset q_t g' (\bar{U}'_L \gamma^\mu U'_L + \bar{U}'_R \gamma^\mu U'_R) Z'_\mu - \left(\sum_i \lambda_{ii} \bar{Q}_{iL} \tilde{H} u_{iR} + \lambda_{4i} \bar{U}'_L u_{iR} \Phi_t + \mu \bar{U}'_L U'_R + \text{h.c.} \right), \quad (2.3)$$

where g' denotes the $U(1)'$ gauge coupling, and $Q_{iL} = (u_{iL}, d_{iL})^T$ and u_{iR} ($i = 1, 2, 3$) stand for the i -th generation of the left-handed quark doublet and the right-handed quark singlet of the SM, respectively. As discussed in refs. [30, 31], mixings of $U'_{L/R}$ with the first two generations suffer from severe experimental constraints. As a consequence, such mixings are assumed to be small compared to its mixing with the third generation and can be therefore neglected, as done in refs. [29, 32]; this leads us to set $\lambda_{41} = \lambda_{42} = 0$. In the following, we will use the abbreviations $\lambda_H = \lambda_{33}$ and $\lambda_{\Phi_t} = \lambda_{43}$.

The fermions present in eq. (2.3) are all given in the interaction eigenbasis. Without loss of generality, we have chosen the basis where the up-type Yukawa matrix is diagonal in the 3×3 SM flavor space. After the EW and the $U(1)'$ symmetry breaking, the mass matrix for the up-type quarks takes the form

$$\begin{pmatrix} \lambda_{11} v_H & 0 & 0 & 0 \\ 0 & \lambda_{22} v_H & 0 & 0 \\ 0 & 0 & \lambda_H v_H & 0 \\ 0 & 0 & \lambda_{\Phi_t} v_{\Phi_t} & \sqrt{2}\mu \end{pmatrix}, \quad (2.4)$$

where the vacuum expectation values (vevs) of H and Φ_t fields are defined by $\langle H \rangle = v_H/\sqrt{2}$ and $\langle \Phi_t \rangle = v_{\Phi_t}/\sqrt{2}$, respectively. When diagonalizing the mass matrix, only the rotation between u_3 and U' is needed in the up sector, and the CKM matrix is defined by the rotation among the down-type quarks. We refer the readers to refs. [30, 31] for more details. As a result, the physical top quarks (t_L, t_R) and their partners (T_L, T_R) are related to the fermions present in eq. (2.3) through [32]

$$\begin{pmatrix} t_L \\ T_L \end{pmatrix} = R(\theta_L) \begin{pmatrix} u_{3L} \\ U'_L \end{pmatrix}, \quad \begin{pmatrix} t_R \\ T_R \end{pmatrix} = R(\theta_R) \begin{pmatrix} u_{3R} \\ U'_R \end{pmatrix}, \quad (2.5)$$

with the rotation matrix given by

$$R(\theta) = \begin{pmatrix} \cos \theta & -\sin \theta \\ \sin \theta & \cos \theta \end{pmatrix}, \quad (2.6)$$

where the mixing angles θ_L and θ_R parameterize the rotation matrices of the left- and right-handed quarks, respectively. In terms of the physical parameters, the top-quark mass m_t , the top-partner mass m_T and the two mixing angles are related to each other through

$$\tan \theta_L = \frac{m_t}{m_T} \tan \theta_R, \quad (2.7)$$

with m_t and m_T determined by

$$\lambda_H = \frac{\cos \theta_L}{\cos \theta_R} \frac{\sqrt{2} m_t}{v_H}, \quad (2.8)$$

$$\lambda_{\Phi_t} = \cos \theta_L \sin \theta_R \frac{\sqrt{2} m_T}{v_{\Phi_t}} \left(1 - \frac{m_t^2}{m_T^2} \right). \quad (2.9)$$

In the fermion mass eigenbasis, the gauge interactions involving the top quark and the top partner take the form [29, 32]

$$\mathcal{L}_\gamma^t = \frac{2}{3} e \bar{t} A t + \frac{2}{3} e \bar{T} A T, \quad (2.10)$$

$$\mathcal{L}_W^t = \frac{g}{\sqrt{2}} V_{td_i} (c_L \bar{t} \bar{W} P_L d_i + s_L \bar{T} \bar{W} P_L d_i) + \text{h.c.}, \quad (2.11)$$

$$\mathcal{L}_Z^t = \frac{g}{c_W} (\bar{t}_L, \bar{T}_L) \begin{pmatrix} \frac{1}{2} c_L^2 - \frac{2}{3} s_W^2 & \frac{1}{2} s_L c_L \\ \frac{1}{2} s_L c_L & \frac{1}{2} s_L^2 - \frac{2}{3} s_W^2 \end{pmatrix} \not{Z} \begin{pmatrix} t_L \\ T_L \end{pmatrix} + \frac{g}{c_W} (\bar{t}_R, \bar{T}_R) \begin{pmatrix} -\frac{2}{3} s_W^2 \end{pmatrix} \not{Z} \begin{pmatrix} t_R \\ T_R \end{pmatrix}, \quad (2.12)$$

$$\mathcal{L}_{Z'}^t = g_t (\bar{t}_L, \bar{T}_L) \begin{pmatrix} s_L^2 & -s_L c_L \\ -s_L c_L & c_L^2 \end{pmatrix} \not{Z}' \begin{pmatrix} t_L \\ T_L \end{pmatrix} + (L \rightarrow R), \quad (2.13)$$

where g is the SM weak coupling constant, $g_t = q_t g'$, $c_{L,R} = \cos \theta_{L,R}$, $s_{L,R} = \sin \theta_{L,R}$, and $s_W = \sin \theta_W$ with θ_W being the Weinberg angle; $d_i \in \{d, s, b\}$ denote the down-type quarks and V_{td_i} the CKM matrix elements. In eq. (2.11), V_{td_i} arise from the rotation among the left-handed down-type quarks, while c_L and s_L from the rotation specified by eq. (2.5). The scalar interactions involving the top quark and the top partner can be written as

$$\mathcal{L}_h^t = -\frac{m_t}{v_H} (\bar{t}_L, \bar{T}_L) \begin{pmatrix} c_L^2 & c_L^2 \tan \theta_R \\ s_L c_L & s_L c_L \tan \theta_R \end{pmatrix} h \begin{pmatrix} t_R \\ T_R \end{pmatrix} + \text{h.c.}, \quad (2.14)$$

$$\mathcal{L}_{\Phi_t} = -\frac{\lambda_{\Phi_t}}{\sqrt{2}} (\bar{t}_L, \bar{T}_L) \begin{pmatrix} -s_L c_R & s_L s_R \\ c_L c_R & c_L s_R \end{pmatrix} h \begin{pmatrix} t_R \\ T_R \end{pmatrix} + \text{h.c.} \quad (2.15)$$

Except for the interactions involving Z' and Φ_t , the quark sector of this model is similar to that of the generic vector-like quark models, which have been extensively studied in the literature [33–42].

2.2 Lepton sector

In the lepton sector, the model is based on the $U(1)_{L_\mu-L_\tau}$ gauge symmetry [43, 44]. Both the second- and the third-generation leptons are charged under the $U(1)'$ gauge group. Explicitly, their quantum numbers under the $SU(3)_C \otimes SU(2)_L \otimes U(1)_Y \otimes U(1)'$ gauge symmetry are given by

$$\begin{aligned} L_{2L} &= (\mathbf{1}, \mathbf{2}, -1/2, +q_\ell), & e_{2R} &= (\mathbf{1}, \mathbf{1}, -1, +q_\ell), \\ L_{3L} &= (\mathbf{1}, \mathbf{2}, -1/2, -q_\ell), & e_{3R} &= (\mathbf{1}, \mathbf{1}, -1, -q_\ell), \end{aligned} \quad (2.16)$$

where L_{2L} and e_{2R} (L_{3L} and e_{3R}) denote the second-generation (third-generation) left-handed lepton doublet and right-handed lepton singlet of the SM, respectively. q_ℓ denotes the charge of the $U(1)'$ gauge symmetry. We also introduce a vector-like muon partner

$$E_{L/R} = (\mathbf{1}, \mathbf{1}, -1, 0), \quad (2.17)$$

as well as two complex scalar fields

$$\phi = (\mathbf{1}, \mathbf{1}, 0, 0), \quad \Phi_\ell = (\mathbf{1}, \mathbf{1}, 0, -q_\ell). \quad (2.18)$$

After spontaneous symmetry breaking, the field ϕ provides mass to the muon partner, while the field Φ_ℓ induces mixing between the muon lepton and the muon partner.

The general Lagrangian involving the Z' boson and the scalars H , Φ_ℓ and ϕ is given by

$$\begin{aligned} \mathcal{L} \supset & q_\ell g' (\bar{L}_{2L} \gamma^\mu L_{2L} + \bar{e}_{2R} \gamma^\mu e_{2R} - \bar{L}_{3L} \gamma^\mu L_{3L} - \bar{e}_{3R} \gamma^\mu e_{3R}) Z'_\mu \\ & - \left[\sum_i \lambda_{ii}^\ell \bar{L}_{iL} H e_{iR} + \lambda_{42}^\ell \bar{E}_L e_{2R} \Phi_\ell + \lambda_{43}^\ell \bar{E}_L e_{3R} \Phi_\ell^* + (\lambda_{41}^\ell \bar{E}_L e_{1R} + \lambda_{44}^\ell \bar{E}_L E_R) \phi + \text{h.c.} \right], \end{aligned} \quad (2.19)$$

where $L_{iL} = (\nu_{iL}, e_{iL})^T$ and e_{iR} ($i = 1, 2, 3$) are the i -th generation of the SM left-handed lepton doublet and right-handed lepton singlet, respectively. Here, for simplicity, we assume that the mixings of $E_{L/R}$ with the first and third generations are small and can be therefore neglected, *i.e.*, $\lambda_{43}^\ell = \lambda_{41}^\ell = 0$. The abbreviations $\eta_H = \lambda_{22}^\ell$, $\lambda_{\Phi_\ell} = \lambda_{42}^\ell$ and $\lambda_\phi = \lambda_{44}^\ell$ will be used in the following.

In eq. (2.19), the fermions are all given in the interaction eigenbasis. After the EW and the $U(1)'$ symmetry breaking, where the scalars H , Φ_ℓ and ϕ acquire their vevs, the resulting mass matrix for the charged leptons is similar to eq. (2.4). After diagonalization, the physical muons (μ_L, μ_R) and their partners (M_L, M_R) can be expressed as

$$\begin{pmatrix} \mu_L \\ M_L \end{pmatrix} = R(\delta_L) \begin{pmatrix} e_{2L} \\ E_L \end{pmatrix}, \quad \begin{pmatrix} \mu_R \\ M_R \end{pmatrix} = R(\delta_R) \begin{pmatrix} e_{2R} \\ E_R \end{pmatrix}, \quad (2.20)$$

where the mixing angles δ_L and δ_R parameterize the rotation matrices of the left- and right-handed leptons, respectively. The two mixing angles are related to each other through

$$\tan \delta_L = \frac{m_\mu}{m_M} \tan \delta_R, \quad (2.21)$$

where m_μ and m_M denote the muon and the muon-partner mass, respectively. Together with the mixing angles and the vevs of H , Φ_ℓ and ϕ , the physical masses m_μ and m_M can be expressed in terms of the Yukawa couplings η_H , λ_{Φ_ℓ} and λ_ϕ as

$$m_\mu = \frac{1}{\sqrt{2}} (\cos \delta_L \cos \delta_R v_H \eta_H - \sin \delta_L \cos \delta_R v_{\Phi_\ell} \lambda_{\Phi_\ell} + \sin \delta_L \sin \delta_R v_\phi \lambda_\phi), \quad (2.22)$$

$$m_M = \frac{1}{\sqrt{2}} (\sin \delta_L \sin \delta_R v_H \eta_H + \cos \delta_L \sin \delta_R v_{\Phi_\ell} \lambda_{\Phi_\ell} + \cos \delta_L \cos \delta_R v_\phi \lambda_\phi), \quad (2.23)$$

and vice versa as

$$\eta_H = \frac{\cos \delta_L}{\cos \delta_R} \frac{\sqrt{2} m_\mu}{v_H}, \quad (2.24)$$

$$\lambda_{\Phi_\ell} = \cos \delta_L \sin \delta_R \frac{\sqrt{2} m_M}{v_{\Phi_\ell}} \left(1 - \frac{m_\mu^2}{m_M^2} \right), \quad (2.25)$$

$$\lambda_\phi = \frac{\cos \delta_R}{\cos \delta_L} \frac{\sqrt{2} m_M}{v_\phi}, \quad (2.26)$$

where $v_{\Phi_\ell} = \sqrt{2} \langle \Phi_\ell \rangle$, $v_\phi = \sqrt{2} \langle \phi \rangle$, and v_H is the vev of the SM Higgs doublet.

In the fermion mass eigenbasis, explicit expressions of the gauge interactions involving the muon and the muon partner can be written as

$$\mathcal{L}_\gamma^\ell = -e \bar{\mu} A \mu - e \bar{M} A M, \quad (2.27)$$

$$\mathcal{L}_W^\ell = \frac{g}{\sqrt{2}} (\hat{c}_L \bar{\mu} W P_L \nu_\mu + \hat{s}_L \bar{M} W P_L \nu_\mu) + \text{h.c.}, \quad (2.28)$$

$$\mathcal{L}_Z^\ell = \frac{g}{c_W} (\bar{\mu}_L, \bar{M}_L) \begin{pmatrix} -\frac{1}{2} \hat{c}_L^2 + s_W^2 & -\frac{1}{2} \hat{s}_L \hat{c}_L \\ -\frac{1}{2} \hat{s}_L \hat{c}_L & -\frac{1}{2} \hat{s}_L^2 + s_W^2 \end{pmatrix} \not{Z} \begin{pmatrix} \mu_L \\ M_L \end{pmatrix} + \frac{g}{c_W} s_W^2 (\bar{\mu}_R, \bar{M}_R) \not{Z} \begin{pmatrix} \mu_R \\ M_R \end{pmatrix}, \quad (2.29)$$

$$\begin{aligned} \mathcal{L}_{Z'}^\ell = & \left[g_\ell (\bar{\mu}_L, \bar{M}_L) \begin{pmatrix} \hat{c}_L^2 & \hat{s}_L \hat{c}_L \\ \hat{s}_L \hat{c}_L & \hat{s}_L^2 \end{pmatrix} \not{Z}' \begin{pmatrix} \mu_L \\ M_L \end{pmatrix} - g_\ell \bar{\tau}_L \not{Z}' \tau_L + (L \rightarrow R) \right] \\ & + g_\ell (\bar{\nu}_\mu \not{Z}' P_L \nu_\mu - \bar{\nu}_\tau \not{Z}' P_L \nu_\tau), \end{aligned} \quad (2.30)$$

where $g_\ell = q_\ell g'$, $\hat{s}_{L,R} = \sin \delta_{L,R}$ and $\hat{c}_{L,R} = \cos \delta_{L,R}$. The Yukawa interactions of the scalars with the muon and the muon partner are given by

$$\mathcal{L}_h = -\frac{m_\mu}{v_H} (\bar{\mu}_L, \bar{M}_L) \begin{pmatrix} \hat{c}_L^2 & \hat{c}_L^2 \tan \delta_R \\ \hat{s}_L \hat{c}_L & \hat{s}_L \hat{c}_L \tan \delta_R \end{pmatrix} h \begin{pmatrix} \mu_R \\ M_R \end{pmatrix} + \text{h.c.}, \quad (2.31)$$

$$\mathcal{L}_{\Phi_\ell} = -\frac{\lambda_{\Phi_\ell}}{\sqrt{2}} (\bar{\mu}_L, \bar{M}_L) \begin{pmatrix} -\hat{s}_L \hat{c}_R & -\hat{s}_L \hat{s}_R \\ \hat{c}_L \hat{c}_R & \hat{c}_L \hat{s}_R \end{pmatrix} \Phi_\ell \begin{pmatrix} \mu_R \\ M_R \end{pmatrix} + \text{h.c.}, \quad (2.32)$$

$$\mathcal{L}_\phi = -\frac{\lambda_\phi}{\sqrt{2}} (\bar{\mu}_L, \bar{M}_L) \begin{pmatrix} \hat{s}_L \hat{s}_R & -\hat{s}_L \hat{c}_R \\ -\hat{c}_L \hat{s}_R & \hat{c}_L \hat{c}_R \end{pmatrix} \phi \begin{pmatrix} \mu_R \\ M_R \end{pmatrix} + \text{h.c.}, \quad (2.33)$$

where h , Φ_ℓ and ϕ denote the physical scalar fields after spontaneous symmetry breaking.

2.3 Choice of the model parameters

To complete our model, we also need to specify the scalar potential, which is given by

$$\begin{aligned} \mathcal{V} = & \sum_S \left[\mu_S^2 |S|^2 + \text{Re}(\lambda_S^{(3)} \phi) |S|^2 - \lambda_S^{(4)} |S|^4 \right] \\ & + (\lambda_{H\phi} |\phi|^2 + \lambda_{H\Phi_t} |\Phi_t|^2 + \lambda_{H\Phi_\ell} |\Phi_\ell|^2) H^\dagger H + (\lambda_{\phi\Phi_t} |\Phi_t|^2 + \lambda_{\phi\Phi_\ell} |\Phi_\ell|^2) |\phi|^2 + \lambda_{\Phi_t\Phi_\ell} |\Phi_t|^2 |\Phi_\ell|^2, \end{aligned} \quad (2.34)$$

where $S \in \{H, \phi, \Phi_t, \Phi_\ell\}$. The potential is assumed to be such that all the scalar fields acquire only real vevs. The scalar fields Φ_t and Φ_ℓ are responsible for the spontaneous breaking of the $U(1)'$ gauge symmetry, and give mass to the Z' boson, with $m_{Z'}^2 = g'^2 (v_{\Phi_t}^2 + v_{\Phi_\ell}^2)$.

In this paper, we focus on the parameter region with $m_T > m_t$ and $m_M > m_\mu$. In the quark sector, without loss of generality, the parameters λ_H , v_H and μ are chosen to be positive. After taking into account the relations in eqs. (2.8) and (2.9), the cases with $v_{\Phi_t} > 0$ and $v_{\Phi_\ell} < 0$ correspond to the ranges of $0 \leq \theta_L < \theta_R < \pi/2$ and $\pi/2 < \theta_R < \theta_L \leq \pi$, respectively. Similarly,

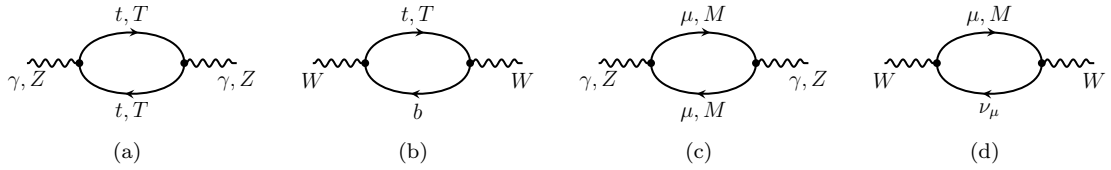


Figure 1: One-loop Feynman diagrams for the vacuum polarizations of gauge bosons in our model.

in the lepton sector, the parameters η_H , λ_{Φ_ℓ} and λ_ϕ are also chosen to be positive. Considering the relations in eqs. (2.24)–(2.26), we find that $v_\phi > 0$, and the cases with $v_{\Phi_\ell} > 0$ and $v_{\Phi_\ell} < 0$ correspond to the ranges of $0 \leq \delta_L < \delta_R < \pi/2$ and $\pi/2 < \delta_R < \delta_L \leq \pi$, respectively. In the following analysis, we will focus on the case where all the vevs are positive and the mixing angles are restricted within the regions of $0 \leq \theta_L < \theta_R < \pi/2$ and $0 \leq \delta_L < \delta_R < \pi/2$.

3 Theoretical framework

In this section, we investigate the relevant observables affected by our model, including the W -boson mass, the $(g-2)_\mu$, the $b \rightarrow s\ell^+\ell^-$ processes, as well as the $Z\mu^+\mu^-$ couplings. The NP contributions to most of them arise at the loop level. During our evaluations, all the loop diagrams are calculated in the unitary gauge. As in ref. [28], the computations are implemented in two independent methods by using different packages including FeynRules [45], FeynArts [46], FeynCalc [47–49], Package-X [50], as well as some in-house routines.

3.1 W -mass shift and oblique parameters

The global fit to the EW precision data, known as the global EW fit [51–53], is a powerful tool to test the SM as well as to probe possible NP effects [54–57]. As an important EW precision observable, the W -boson mass in the SM is determined from the global EW fit. Recently, the CDF m_W measurement [11] shows large deviation from the SM prediction, which could be explained by NP contributions; see *e.g.* refs. [58–65] and the references therein. In our model, the W -boson mass shift can be divided into the following three parts:

$$\Delta m_W = \Delta m_W^Q + \Delta m_W^L + \Delta m_W^{W\mu\nu}, \quad (3.1)$$

where Δm_W^Q , Δm_W^L and $\Delta m_W^{W\mu\nu}$ denote the contributions from the top-partner, the muon-partner and the modified $W\mu\nu$ vertex, respectively. We show in figure 1 the relevant one-loop Feynman diagrams for these NP contributions.

The oblique parameters S , T and U encode most of the NP effects on the SM EW sector [66–68]. To be specific, these parameters capture the NP contributions from the gauge-boson vacuum-polarization corrections and can be generically written as [66, 67]

$$\begin{aligned} S &= \frac{4s_W^2 c_W^2}{\alpha_e} \left[\frac{\Pi_{ZZ}(m_Z^2) - \Pi_{ZZ}(0)}{m_Z^2} - \frac{c_W^2 - s_W^2}{s_W c_W} \Pi'_{Z\gamma}(0) - \Pi'_{\gamma\gamma}(0) \right], \\ T &= \frac{1}{\alpha_e} \left[\frac{\Pi_{WW}(0)}{m_W^2} - \frac{\Pi_{ZZ}(0)}{m_Z^2} \right], \\ U &= \frac{4s_W^2}{\alpha_e} \left[\frac{\Pi_{WW}(m_W^2) - \Pi_{WW}(0)}{m_W^2} - \frac{c_W}{s_W} \Pi'_{Z\gamma}(0) - \Pi'_{\gamma\gamma}(0) \right] - S, \end{aligned}$$

where Π_{XY} denotes the vacuum polarization of the gauge fields with $X, Y = W, Z, \gamma$, $c_W = \cos\theta_W$, and α_e is the fine structure constant. In terms of these oblique parameters, the W -boson mass shift

can be written as [66]

$$\Delta m_W^2 = \frac{\alpha_e c_W^2 m_Z^2}{c_W^2 - s_W^2} \left[-\frac{S}{2} + c_W^2 T + \frac{c_W^2 - s_W^2}{4s_W^2} U \right]. \quad (3.2)$$

Therefore, to explain the discrepancy of the CDF m_W measurement from the SM expectation, we need a global EW fit to the oblique parameters S , T and U , which could be affected by contributions from both the quark and the lepton sector in our model. Let us discuss them in turn.

In the model introduced in section 2, extra contributions to the vacuum polarizations of gauge fields arise from the diagrams shown in figure 1. Figures 1a and 1b encode the contributions from the modified quark-gauge couplings that are characterized by the mixing angle θ_L and the loops involving the top partner, respectively. Their contributions to the oblique parameters read [28]

$$S_Q = \frac{s_L^2}{12\pi} \left[K_1(y_t, y_T) + 3c_L^2 K_2(y_t, y_T) \right], \quad (3.3)$$

$$T_Q = \frac{3s_L^2}{16\pi s_W^2} \left[x_T - x_t - c_L^2 \left(x_T + x_t + \frac{2x_t x_T}{x_T - x_t} \ln \frac{x_t}{x_T} \right) \right], \quad (3.4)$$

$$U_Q = \frac{s_L^2}{12\pi} \left[K_3(x_t, y_t) - K_3(x_T, y_T) \right] - S_Q, \quad (3.5)$$

where $x_q = m_q^2/m_W^2$ and $y_q = m_q^2/m_Z^2$ for $q = t, T$. Explicit expressions of the loop functions $K_{1,2,3}(x, y)$ are recapitulated in appendix C.

Similar to the quark sector, contributions from the lepton sector arise from figures 1c and 1d. Their contributions to the oblique parameters can be written as

$$S_L = \frac{\hat{s}_L^2}{12\pi} \left[K_4(y_\mu, y_M) + \hat{c}_L^2 K_5(y_\mu, y_M) \right], \quad (3.6)$$

$$T_L = \frac{\hat{s}_L^2}{16\pi \hat{s}_W^2} \left[x_M - x_\mu - \hat{c}_L^2 \left(x_M + x_\mu + \frac{2x_\mu x_M}{x_M - x_\mu} \ln \frac{x_\mu}{x_M} \right) \right], \quad (3.7)$$

$$U_L = \frac{\hat{s}_L^2}{12\pi} \left[K_6(x_\mu, y_\mu) - K_6(x_M, y_M) \right] - S_L, \quad (3.8)$$

where $x_\ell = m_\ell^2/m_W^2$ and $y_\ell = m_\ell^2/m_Z^2$ for $\ell = \mu, M$, $\hat{s}_L = \sin \delta_L$ and $\hat{c}_L = \cos \delta_L$. Explicit expressions of the loop functions $K_{4,5,6}(x, y)$ are listed in appendix C. From eqs. (3.6)–(3.8) (eqs. (3.3)–(3.5)), one can see that the contributions to the oblique parameters S , T and U from the lepton (quark) sector are solely determined by the two NP parameters δ_L and m_M (θ_L and m_T) and are proportional to $\sin^2 \delta_L$ ($\sin^2 \theta_L$).

Finally, let us discuss the last term of eq. (3.1), $\Delta m_W^{W\mu\nu}$, which is induced by the modified $W\mu\nu$ coupling and characterized by the mixing angle δ_L , as given in eq. (2.28). The modified $W\mu\nu$ coupling can affect the muon lifetime, from which the Fermi constant G_F is extracted. During the global EW fit, the prediction for m_W is obtained from its relation to G_F . This implies that the input G_F used for calculating m_W should be the modified one rather than the one given by the Particle Data Group (PDG) [1]. Therefore, the NP correction to the $W\mu\nu$ coupling indirectly translates to a shift of the W -boson mass, $\Delta m_W^{W\mu\nu}$, which can be written as [69–71]

$$\frac{(m_W^{\text{SM}} + \Delta m_W^{W\mu\nu})^2}{m_Z^2} = \frac{1}{2} + \sqrt{\frac{1}{4} - \frac{\pi\alpha_e}{\sqrt{2}G_F m_Z^2}} |1 + \Delta r|, \quad (3.9)$$

where Δr encodes the NP correction to the muon lifetime. Specific to our model, the modified $W\mu\nu$ coupling results in $\Delta r = \cos \delta_L - 1$.

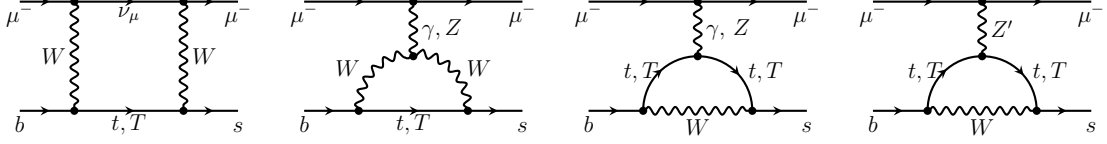


Figure 2: One-loop Feynman diagrams for the $b \rightarrow s\mu^+\mu^-$ transitions, including the Z' and T contributions, as well as the effects of the modified $Z\mu\mu$, $W\mu\nu$ and Wtb couplings.

3.2 $b \rightarrow s\ell^+\ell^-$ transitions

Our model can also be efficiently explored through the quark-level $b \rightarrow s\ell^+\ell^-$ transitions, such as the $B \rightarrow K^{(*)}\ell^+\ell^-$, $B_s \rightarrow \ell^+\ell^-$ and $B_s \rightarrow \phi\ell^+\ell^-$ decays. Here the NP contributions arise firstly at the one-loop level, with the relevant Feynman diagrams shown in figure 2. As found already in ref. [28], the NP contributes only to the short-distance Wilson coefficients \mathcal{C}_9 and \mathcal{C}_{10} of the low-energy effective Hamiltonian governing the $b \rightarrow s\ell^+\ell^-$ transitions [72]

$$\mathcal{H}_{\text{eff}} \supset -\frac{4G_F}{\sqrt{2}} V_{tb}V_{ts}^* \frac{\alpha_e}{4\pi} (\mathcal{C}_{9\ell}\mathcal{O}_{9\ell} + \mathcal{C}_{10\ell}\mathcal{O}_{10\ell}) + \text{h.c.}, \quad (3.10)$$

with the two semi-leptonic operators given by $\mathcal{O}_{9\ell} = (\bar{s}\gamma^\mu P_L b) (\bar{\ell}\gamma_\mu \ell)$ and $\mathcal{O}_{10\ell} = (\bar{s}\gamma^\mu P_L b) (\bar{\ell}\gamma_\mu \gamma_5 \ell)$, respectively. The NP contributions to $\mathcal{C}_{9\ell}$ and $\mathcal{C}_{10\ell}$ can be divided into the Lepton-Flavor Universal (LFU) and the Lepton-Flavor Violating (LFV) parts. The former arise from the diagrams with the SM gauge bosons, and are given by

$$\mathcal{C}_{9\ell}^{\text{NP}} = s_L^2 I_1 + s_L^2 \left(1 - \frac{1}{4s_W^2}\right) (I_2 + c_L^2 I_3), \quad (3.11)$$

$$\mathcal{C}_{10\ell}^{\text{NP}} = \frac{s_L^2}{4s_W^2} (I_2 + c_L^2 I_3), \quad (3.12)$$

with $s_{L,R} = \sin\theta_{L,R}$ and $c_{L,R} = \cos\theta_{L,R}$. They are proportional to $\sin^2\theta_L$. The LFV contributions can be written as

$$\mathcal{C}_{9\mu}^{\text{NP}} = \Delta\mathcal{C}_+^{W,Z} + \Delta\mathcal{C}_+^{Z'}, \quad (3.13)$$

$$\mathcal{C}_{10\mu}^{\text{NP}} = \Delta\mathcal{C}_-^{W,Z} + \Delta\mathcal{C}_-^{Z'}, \quad (3.14)$$

with

$$\Delta\mathcal{C}_\pm^{W,Z} = \pm \frac{\hat{s}_L^2 s_L^2}{8s_W^2} (I_6 + c_L^2 I_7), \quad (3.15)$$

$$\Delta\mathcal{C}_\pm^{Z'} = \frac{(\hat{c}_R^2 \pm \hat{c}_L^2) g_\ell g_t}{e^2} \frac{m_W^2}{m_{Z'}^2} c_L^2 s_R^2 \left(I_4 - \frac{c_L^2}{c_R^2} I_5 \right), \quad (3.16)$$

where $g_\ell = q_\ell g'$, $g_t = q_t g'$, $\hat{s}_{L,R} = \sin\delta_{L,R}$ and $\hat{c}_{L,R} = \cos\delta_{L,R}$. Here the contributions $\Delta\mathcal{C}_\pm^{W,Z}$ arise from the diagrams involving the W and Z bosons, while $\Delta\mathcal{C}_\pm^{Z'}$ from the Z' -penguin diagrams. In our case of small mixing angles θ_L and δ_L , as will be demonstrated in section 4, $\Delta\mathcal{C}_\pm^{W,Z}$ will be highly suppressed because they are proportional to $\hat{s}_L^2 s_L^2 = \sin^2\delta_L \sin^2\theta_L$. Thus, we can safely take the approximations $\mathcal{C}_{9e}^{\text{NP}} \approx \mathcal{C}_{10e}^{\text{NP}} \approx 0$ and $(\mathcal{C}_{9\mu}^{\text{NP}}, \mathcal{C}_{10\mu}^{\text{NP}}) \approx (\Delta\mathcal{C}_+^{Z'}, \Delta\mathcal{C}_-^{Z'})$. The loop integrals I_{1-7} are functions of $m_{t,T}$ and $m_{\mu,M}$, whose explicit expressions are given in appendix C. Keeping only the leading terms in $\sin\theta_R$ and m_W^2/m_T^2 , our results are in agreement with that obtained in ref. [32].

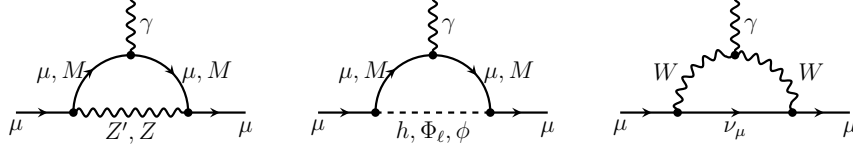


Figure 3: One-loop Feynman diagrams for the muon ($g-2$), including the Z' , Φ_ℓ and ϕ contributions, as well as the effects of the modified $Z\mu\mu$, $h\mu\mu$ and $W\mu\nu$ couplings.

3.3 Muon $g-2$

The muon anomalous magnetic moment $a_\mu \equiv (g-2)_\mu/2$ can provide very promising probes of potential NP effects [4, 73]. Specific to our model, the observable a_μ is affected by the one-loop Feynman diagrams shown in figure 3, which involve the Z' , ϕ and Φ_ℓ bosons, as well as the SM diagrams but with the modified $Z\mu\mu$, $h\mu\mu$ and $W\mu\nu$ couplings. Their total contributions to Δa_μ can be written as

$$\Delta a_\mu = \Delta a_\mu^{Z'} + \Delta a_\mu^\phi + \Delta a_\mu^{\Phi_\ell} + \Delta a_\mu^W + \Delta a_\mu^Z + \Delta a_\mu^h, \quad (3.17)$$

where $\Delta a_\mu^i = \Delta a_\mu^{i,\mu} + \Delta a_\mu^{i,M}$ ($i = Z, Z', \phi, \Phi_\ell$), and $\Delta a_\mu^{i,j}$ ($j = \mu, M$) denotes the contribution from the diagrams involving the particles i and j . Their explicit expressions are given, respectively, by

$$\Delta a_\mu^{Z,\mu} = -\frac{g^2 w_\mu (\hat{c}_L^4 - 2\hat{s}_L^2 \hat{s}_W^2 - 1)}{48\pi^2 c_W^2}, \quad (3.18)$$

$$\Delta a_\mu^{Z,M} = -\frac{\hat{c}_L^2 \hat{s}_L^2 w_\mu g^2 (5w_M^4 - 14w_M^3 + 39w_M^2 - 38w_M + 8 - 18w_M^2 \ln w_M)}{384\pi^2 c_W^2 (w_M - 1)^4}, \quad (3.19)$$

$$\Delta a_\mu^{Z',\mu} = -\frac{g_\ell^2 x_\mu (\hat{c}_L^4 - 3\hat{c}_L^2 \hat{c}_R^2 + \hat{c}_R^4)}{12\pi^2}, \quad (3.20)$$

$$\Delta a_\mu^{Z',M} = \frac{\hat{s}_L^2 \hat{c}_R^2 g_\ell^2 x_M (x_M^3 + 3x_M - 4 - 6x_M \ln x_M)}{16\pi^2 (x_M - 1)^3}, \quad (3.21)$$

$$\Delta a_\mu^{\phi,\mu} = \frac{\hat{s}_L^2 \hat{s}_R^2 \lambda_\phi^2}{32\pi^2} f_s(z_\mu), \quad (3.22)$$

$$\Delta a_\mu^{\phi,M} = \frac{\hat{s}_L^2 \hat{c}_R^2 \lambda_\phi^2 z_M (z_M^2 - 4z_M + 3 + 2 \ln z_M)}{32\pi^2 (z_M - 1)^3} + \frac{z_\mu (\hat{c}_R^2 \hat{s}_L^2 + \hat{c}_L^2 \hat{s}_R^2) \lambda_\phi^2 (z_\mu^3 - 6z_\mu^2 + 3z_\mu + 2 + 6x_M \ln z_\mu)}{192\pi^2 (z_M - 1)^4}, \quad (3.23)$$

$$\Delta a_\mu^{\Phi_\ell,\mu} = \frac{\hat{s}_L^2 \hat{c}_R^2 \lambda_{\Phi_\ell}^2}{32\pi^2} f_s(y_\mu), \quad (3.24)$$

$$\Delta a_\mu^{\Phi_\ell,M} = -\frac{\hat{s}_L^2 \hat{c}_R^2 \lambda_{\Phi_\ell}^2 y_M (y_M^2 - 4y_M + 3 + 2 \ln y_M)}{32\pi^2 (y_M - 1)^3}, \quad (3.25)$$

$$\Delta a_\mu^W = -\frac{5\hat{s}_L^2 g^2 w_\mu}{96\pi^2 c_W^2}, \quad (3.26)$$

with

$$f_s(x) = \frac{3x-2}{x} + \frac{(3x-1)}{x^2} \ln x + \frac{2\sqrt{1-4x}(x-1)}{x^2} \ln \frac{1+\sqrt{1-4x}}{2\sqrt{x}}, \quad (3.27)$$

where $w_i = m_i^2/m_Z^2$, $x_i = m_i^2/m_{Z'}^2$, $y_i = m_i^2/m_{\Phi_\ell}^2$ and $z_i = m_i^2/m_\phi^2$ ($i = \mu, M$). From these results, one can see that the NP contributions to a_μ will vanish in the limit of $\delta_L \rightarrow 0$ or $\delta_R \rightarrow 0$.

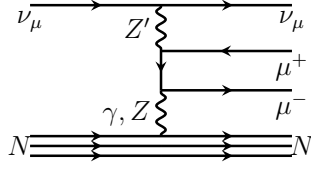


Figure 4: The Z' contribution to the neutrino trident production in our model. The diagram with μ^+ and μ^- reversed is not shown.

3.4 Neutrino trident production

The Z' couplings to muons are significantly constrained by the rare process of neutrino trident production, *i.e.*, the production of a $\mu^+\mu^-$ pair from the scattering of a muon-neutrino with heavy nucleus [74–77]. In our model, the Z' boson contributes to this rare process through the tree-level Feynman diagram shown in figure 4. The ratio of the cross section in our model to that in the SM, $r_{\nu\text{TP}} \equiv \sigma_{\text{NP}}/\sigma_{\text{SM}}$, is calculated to be [32, 78, 79]

$$r_{\nu\text{TP}} = \frac{|g_\ell^2 (\hat{c}_L^2 + \hat{c}_R^2) / m_{Z'}^2 + \sqrt{2} (1 + 4s_W^2) G_F|^2 + |g_\ell^2 (\hat{c}_L^2 - \hat{c}_R^2) / m_{Z'}^2 + \sqrt{2} G_F|^2}{2G_F^2 [1 + (1 + 4s_W^2)^2]}, \quad (3.28)$$

where $g_\ell = g_\ell g'$ and $\hat{c}_{L,R} = \cos \delta_{L,R}$.

3.5 $Z\mu\mu$ and $W\mu\nu$ couplings

Any modification of the Z couplings to leptons must receive stringent constraints from the LEP measurements at the Z pole [80]. In our model, the effective Z couplings to leptons are given by

$$\mathcal{L} = \frac{g}{c_W} \bar{\ell} \not{Z} (g_{L\ell} P_L + g_{R\ell} P_R) \ell, \quad (3.29)$$

with $\ell = \mu$ or e . The effective couplings $g_{L\mu/R\mu}$ include both the tree-level couplings specified by eq. (2.29) and the one-loop vertex corrections shown in figure 5. The latter can be written as

$$\Delta g_{\Gamma\mu} = \Delta g_{\Gamma\mu}^{Z'} + \Delta g_{\Gamma\mu}^{\Phi_\ell} + \Delta g_{\Gamma\mu}^\phi + \Delta g_{\Gamma\mu}^W + \Delta g_{\Gamma\mu}^Z + \Delta g_{\Gamma\mu}^\gamma + \Delta g_{\Gamma\mu}^h + \Delta g_{\Gamma\mu}^{Z-Z'}, \quad (3.30)$$

with $\Gamma = L$ or R . Here $\Delta g_{\Gamma\mu}^i$ denotes the correction from the diagram involving the particle i for $i = Z', \Phi_\ell, \phi, W, Z, \gamma$ and h . As done in ref. [81], these corrections are calculated in the on-shell renormalization scheme. Furthermore, we find that the renormalization of the mixing angle δ_L has to be taken into account. Details of the calculation are given in appendix A. The vertex corrections $\Delta g_{\Gamma\mu}^{Z', \phi, \Phi_\ell}$ depend on $g_\ell, \lambda_{\Phi_\ell}, \lambda_\phi, m_\mu/M, m_{Z'}, m_{\Phi_\ell}, m_\phi$, and their explicit expressions are provided as an ancillary notebook file. In addition, the $Z - Z'$ mixing via the top (top-partner) loops could also affect the $Z\mu\mu$ couplings [28, 82, 83]. Such an effect, denoted by $\Delta g_{\Gamma\mu}^{Z-Z'}$ in eq. (3.29), can be written as

$$\Delta g_{\Gamma\mu}^{Z-Z'} = \frac{3g_t g_\ell s_L^2 \hat{c}_\Gamma^2}{32\pi^2 (m_Z^2 - m_{Z'}^2)} (c_L^2 I_L + c_R^2 I_R), \quad (3.31)$$

where the loop functions $I_{L,R}$ depend on m_t and m_T , and their explicit expressions can be found in appendix C. Finally, the contributions involving the SM particles are all proportional to $\sin^2 \delta_L$. In our numerical analysis, we will consider the case of small mixing angle δ_L to avoid large modification of the $Z\mu\mu$ vertex at the tree level. Therefore, these contributions can be safely neglected, which means that $\Delta g_{\Gamma\mu}^{W,Z,\gamma,h} \approx 0$.

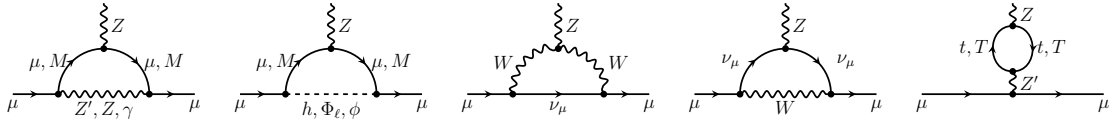


Figure 5: Relevant Feynman diagrams for the one-loop corrections to the $Z\mu\mu$ vertex in our model.

To constrain the $Z\mu\mu$ couplings, we follow refs. [82, 84] and consider the following two observables. The first one is the LFU ratio, $R_{\mu/e}^Z \equiv \Gamma(Z \rightarrow \mu^+\mu^-)/\Gamma(Z \rightarrow e^+e^-)$, measured at LEP-I [80]. Using the effective couplings defined in eq. (3.29), we can write the decay width of $Z \rightarrow \ell^+\ell^-$ as

$$\Gamma(Z \rightarrow \ell^+\ell^-) = \frac{m_Z \lambda_Z^{1/2}}{6\pi v^2} \left[(|g_{L\ell}|^2 + |g_{R\ell}|^2) \left(1 - \frac{m_\ell^2}{m_Z^2}\right) + 6 \frac{m_\ell^2}{m_Z^2} \text{Re}(g_{L\ell} g_{R\ell}^*) \right], \quad (3.32)$$

with $\lambda_Z \equiv m_Z^2(m_Z^2 - 4m_\ell^2)$. The second observable is the leptonic asymmetry parameter defined by [82]

$$\mathcal{A}_\mu = \frac{\Gamma(Z \rightarrow \mu_L^+ \mu_L^-) - \Gamma(Z \rightarrow \mu_R^+ \mu_R^-)}{\Gamma(Z \rightarrow \mu^+ \mu^-)}, \quad (3.33)$$

where $\mu_{L/R}$ corresponds to the left/right-handed muon. Specific to our model, we obtain

$$\Gamma(Z \rightarrow \ell_\Gamma^+ \ell_\Gamma^-) = \frac{m_Z \lambda_Z^{1/2}}{6\pi v^2} |g_{\Gamma\ell}|^2 \left(1 - \frac{m_\ell^2}{m_Z^2}\right), \quad (3.34)$$

for $\Gamma = L$ or R .

From eq. (2.28), one can see that the mixing angle δ_L can change the $W\mu\nu$ coupling, and thus affects the branching ratio of the $W^+ \rightarrow \mu^+\nu$ decay. Explicitly, we have the relation

$$\frac{\mathcal{B}(W^+ \rightarrow \mu^+\nu)}{\mathcal{B}_{\text{SM}}(W^+ \rightarrow \mu^+\nu)} = \cos^2 \delta_L, \quad (3.35)$$

which is valid at the tree level.

4 Numerical analysis

In this section, we proceed to present our numerical results and discussions. Firstly we list in table 2 the main input parameters used in our numerical analysis.

As discussed in section 3, the relevant independent parameters in our model contain, besides the masses of the NP particles, the mixing angles and the couplings $g_t, g_\ell, \lambda_\phi, \lambda_{\Phi_\ell}, \lambda_{\Phi_\ell}$, where the re-definitions $g_\ell = q_\ell g'$ and $g_t = q_t g'$ have been taken. In our numerical analysis, we consider the following parameter space:

$$0 < g_t, g_\ell, \lambda_\phi, \lambda_{\Phi_\ell}, \lambda_{\Phi_\ell} < 2. \quad (4.1)$$

Taking into account the relations specified by eqs. (2.7) and (2.21), we will take θ_L and δ_L as the two independent mixing angles in the quark and lepton sectors, respectively. Their values are varied within the following ranges:

$$0 < \sin \theta_L < 0.5, \quad 0 < \sin \delta_L < 0.01, \quad (4.2)$$

to avoid large tree-level modifications to the W, Z and h couplings to fermions, as will be discussed in detail in the next subsection.

Input	Value	Unit	Ref.
m_t^{pole}	172.69 ± 0.30	GeV	[1]
s_W^2	0.23121		[1]
G_F	1.1663788×10^{-5}	GeV^{-2}	[1]
$\alpha_e(m_Z)$	1/127.940(14)		[1]
$\alpha_s(m_Z)$	0.11843(81)		[85]
$ V_{cb} $	$(41.15 \pm 0.34 \pm 0.45) \times 10^{-3}$		[86]
$ V_{ub} $	$(3.88 \pm 0.08 \pm 0.21) \times 10^{-3}$		[86]
$ V_{us} f_+^{K \rightarrow \pi}(0)$	0.2165 ± 0.0004		[1]
γ	$72.1^{+5.4}_{-5.7}$	°	[86]
$f_+^{K \rightarrow \pi}(0)$	$0.9675 \pm 0.0009 \pm 0.0023$		[86]

Table 2: Main input parameters used in our numerical analysis.

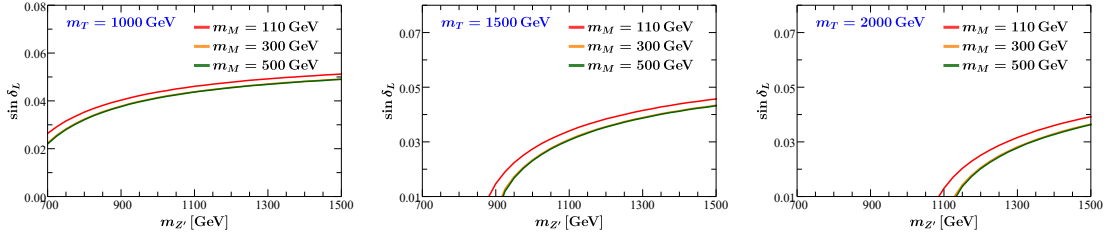


Figure 6: The 2σ upper bounds on $\sin \delta_L$ as a function of $m_{Z'}$ from the measured $Z\mu\mu$ coupling, for $m_M = 110, 300$ and 500 GeV as well as $m_T = 1000, 1500$ and 2000 GeV.

4.1 $Z\mu\mu$ and $W\mu\nu$ couplings

As discussed in section 3.5, the $Z\mu\mu$ coupling is stringently constrained by the LEP measurements [80], especially by the observables $R_{\mu/e}^Z$ and \mathcal{A}_μ . In our model, the $Z\mu\mu$ coupling is affected by the mixing angle δ_L at the tree level, and also receives contributions from the $Z - Z'$ mixing and the vertex corrections at the one-loop level.

In our numerical analysis, we take $g_\ell = g_t = 1$, $\lambda_\phi = \lambda_{\Phi_\ell} = 1$,¹ $m_\phi = 1$ GeV and $m_{\Phi_\ell} = 2$ TeV, which are all consistent with the constraints discussed in the following subsections. The parameter space of $\sin \theta_L$ is chosen within the range allowed by the CDF m_W measurement, as will be derived in section 4.2. Then, the remaining relevant parameters are $(m_{Z'}, m_T, m_M, \sin \delta_L)$. Taking the LEP measurements $R_{\mu/e}^Z = 1.0001 \pm 0.0024$ [1] and $\mathcal{A}_\mu = 0.1456 \pm 0.0091$ [80] as constraints, we can finally obtain the allowed values of these parameters. As an illustration, we show in figure 6 the 2σ upper bounds on $\sin \delta_L$ as a function of $m_{Z'}$ from the measured $Z\mu\mu$ coupling, for $m_M = 110, 300$ and 500 GeV as well as $m_T = 1000, 1500$ and 2000 GeV. It can be seen that a lighter Z' or a heavier T implies a stronger upper bound on $\sin \delta_L$, while the upper bound is not sensitive to m_M . Numerically, we obtain $\sin \delta_L < 0.05$ in the 2σ allowed parameter space. Furthermore, we have checked that, in the 2σ allowed parameter space, the NP contributions to the $Z\mu\mu$ coupling from the $Z - Z'$ mixing and the one-loop vertex corrections are both less than 1% of the SM prediction. This in turn means that the fine-tuning among the different NP contributions is small.

¹We have checked that varying λ_ϕ and λ_{Φ_ℓ} within the range of eq. (4.1) only changes our results slightly.

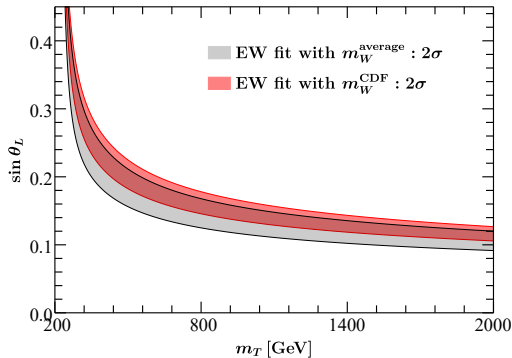


Figure 7: The 2σ allowed regions in the $(m_T, \sin\theta_L)$ plane from the global EW fit. The red and the black region are obtained from the latest CDF measurement m_W^{CDF} [11] and from the average of m_W [65] including both m_W^{CDF} and all the previous measurements [1], respectively.

On the other hand, the mixing angle δ_L receives also constraint from the measured branching ratio of $W^+ \rightarrow \mu^+\nu$ decay, as indicated by eq. (3.35). Taking as input the LEP measurement $\mathcal{B}(W^+ \rightarrow \mu^+\nu)_{\text{exp}} = 0.1063(15)$ [1] and the SM prediction $\mathcal{B}(W^+ \rightarrow \mu^+\nu)_{\text{SM}} = 0.1083$ [87], we obtain the upper bound $\sin\delta_L < 0.43$, which is much weaker than that from the $Z\mu\mu$ coupling.

In the following, we will consider the upper bound $\sin\delta_L < 0.01$, which definitely satisfies the constraint from the $Z\mu\mu$ coupling. In addition, since the $Z\mu\mu$ coupling is not sensitive to m_M , a value of $m_M = 300$ GeV will be taken for simplicity. As will be demonstrated later, such a choice of $\sin\delta_L$ and m_M is enough to explain the muon $g-2$ anomaly and the $b \rightarrow s\ell^+\ell^-$ discrepancies, while satisfying most of the relevant constraints mentioned in section 3.

4.2 W -boson mass and global EW fit

As the NP effects could affect all the three oblique parameters S , T and U , a global EW fit is necessary to see if our model could explain the CDF m_W measurement [11]. Recently, the global EW fit including the latest CDF m_W measurement has been performed by several groups [61–65]. Here we will adopt the result obtained in ref. [64], which is based on the package `Gfitter` [54–56].² The resulting values of the oblique parameters, together with their correlations, read [64]

$$\begin{aligned} S &= 0.06 \pm 0.10, \\ T &= 0.11 \pm 0.12, \\ U &= 0.14 \pm 0.09, \end{aligned} \quad \text{cor} = \begin{bmatrix} 1.00 & 0.90 & -0.59 \\ & 1.00 & -0.85 \\ & & 1.00 \end{bmatrix}, \quad (4.3)$$

where “cor” denotes the correlation matrix.

As discussed in section 3.1, the NP contributions arise mainly from the diagrams involving the top-partner, the muon-partner and the modified $W\mu\nu$ coupling. In the following, we will consider the region of $\sin\delta_L < 0.01$ obtained in the last subsection, and investigate these three contributions one by one.

- By using the input parameters in table 2 and considering $\sin\delta_L < 0.01$, we find that the W -boson mass shift from the modified $W\mu\nu$ coupling (cf. eq. (3.9)) is given numerically by $\Delta m_W^{W\mu\nu} < 0.007$ GeV. Therefore, such an effect is too small to explain the latest CDF m_W measurement [11], and can be safely neglected.

²It is found that using the global EW fit results [65] based on the package `HEPfit` [88] does not substantially change our numerical results.

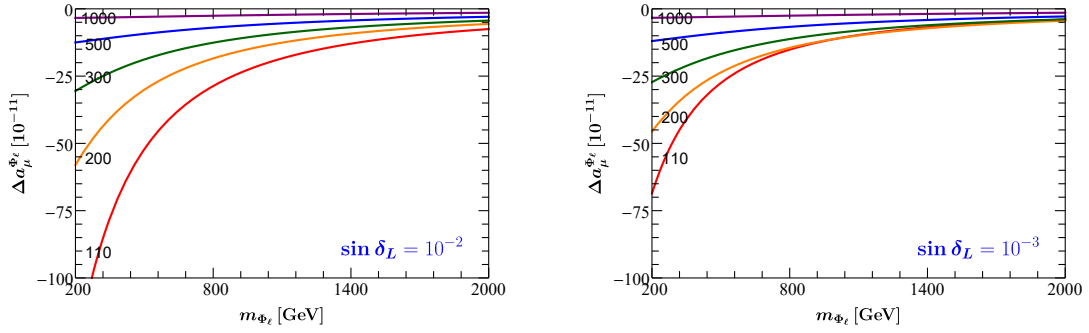


Figure 8: The Φ_ℓ contribution to Δa_μ as a function of m_{Φ_ℓ} for $\sin \delta_L = 10^{-2}$ (left) and 10^{-3} (right), with $m_M = 110, 200, 300, 500$ and 1000 GeV.

- From eqs. (3.6)–(3.8), we can see that the muon-partner contributions to the oblique parameters S , T and U are proportional to $\sin^2 \delta_L$. After considering $\sin \delta_L < 0.01$, the resulting shift Δm_W^M is highly suppressed and found to be $\mathcal{O}(10^{-3})$ smaller than from the top-partner contribution. Therefore, we could also safely neglect the muon-partner contributions.
- The top-partner effects on the S , T and U parameters depend only on the mixing angle θ_L and the top-partner mass m_T (cf. eqs. (3.3)–(3.5)). Here we consider $\sin \theta_L < 0.5$ to avoid large modification to the Wtb coupling. After taking into account the global EW fit results in eq. (4.3), we find that there still exist allowed parameter regions at the 2σ level, as shown in figure 7. It can be inferred that $\sin \theta_L = 0.14 \sim 0.20$ within the mass range $500 < m_T < 2000$ GeV.

Consequently, the latest CDF W -boson mass shift can be explained in our model, and the allowed parameter regions shown in figure 7 will be used in the following numerical analysis. When the parameters vary within the regions, deviations of the top-Higgs coupling (cf. eq. (2.14)) from its SM value are less than 10%, which are also consistent with the current Higgs measurements at the LHC [32, 89–91]. In addition, for comparison, we show in figure 7 the allowed parameter regions by taking as constraint the average of m_W [65] including both m_W^{CDF} and all the previous measurements [1]. In this case, the allowed values of $\sin \theta_L$ become smaller.

4.3 Muon $g - 2$ and neutrino trident production

The $U(1)_{L_\mu - L_\tau}$ extension of the SM can explain the $(g - 2)_\mu$ anomaly, but receives significant constraint from the rare process of neutrino trident production [78]. In this subsection, we will investigate the possibility of explaining the $(g - 2)_\mu$ anomaly in our model, while satisfying the constraint from neutrino trident production. This rare process has been searched for in several neutrino beam experiments, including CHARM-II [74], CCFR [75] and NuTeV [76, 77]. Combining the data from these collaborators, the ratio of the measured cross section to that in the SM is given by $\sigma_{\text{exp}}/\sigma_{\text{SM}} = 0.95 \pm 0.25$ [79], which should be confronted with the theoretical result in eq. (3.28).

The NP contributions to $(g - 2)_\mu$ can be divided into three parts (cf. eq. (3.17)), arising from the penguin diagrams involving Z' , Φ_ℓ and ϕ , respectively. Let us now discuss them one by one.

- From eqs. (3.24)–(3.25), one can see that the Φ_ℓ contribution $\Delta a_\mu^{\Phi_\ell}$ is proportional to $\lambda_{\Phi_\ell}^2$ and depends on the parameters $(m_M, \sin \delta_L, m_{\Phi_\ell})$. Taking $\lambda_{\Phi_\ell} = 1$ for simplicity, we show in figure 8 the resulting $\Delta a_\mu^{\Phi_\ell}$ as a function of m_{Φ_ℓ} for various values of m_M and $\sin \delta_L$. It can be seen that the Φ_ℓ contribution is always negative, which increases the discrepancy of $(g - 2)_\mu$. However, such a negative contribution will be highly suppressed by heavy Φ_ℓ or

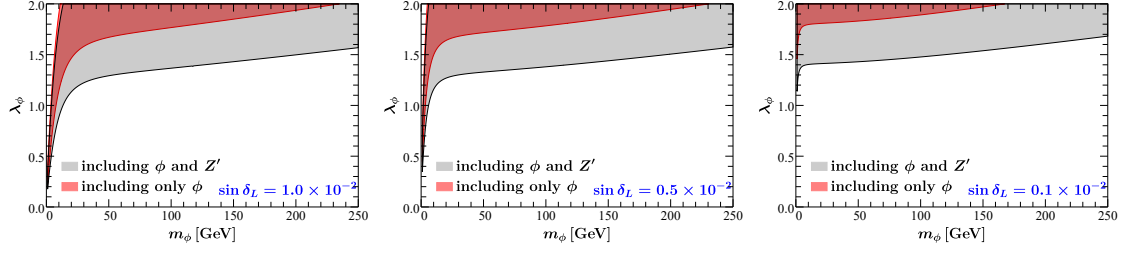


Figure 9: Constraints on (m_ϕ, λ_ϕ) from the $(g-2)_\mu$ for $\sin \delta_L = (1.0, 0.5, 0.1) \times 10^{-2}$. The red and the gray region denote the 2σ allowed parameter space including only the ϕ and both the ϕ and Z' contributions, respectively. For the Z' contribution, $m_{Z'} = 1$ TeV and $g_\ell = 2$ are taken, and the constraint from neutrino trident production has been taken into account.

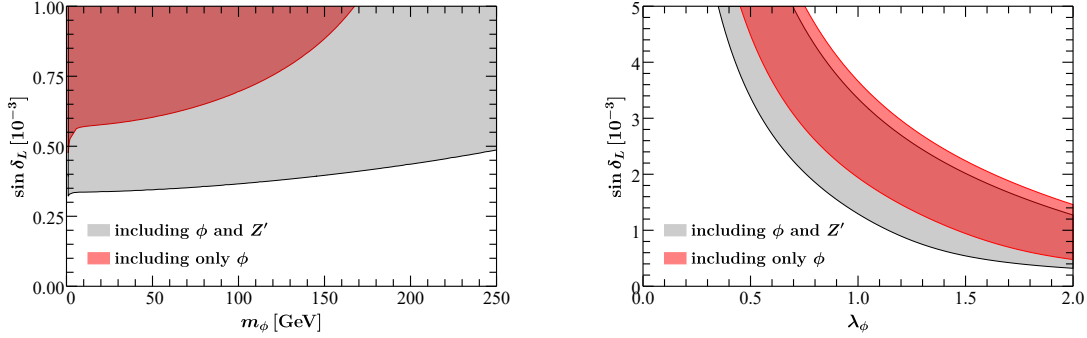


Figure 10: Constraints on $(\sin \delta_L, m_\phi, \lambda_\phi)$ from the $(g-2)_\mu$ at the 2σ level, which are plotted in the $(m_\phi, \sin \delta_L)$ plane for $\lambda_\phi = 2$ (left) and in the $(\lambda_\phi, \sin \delta_L)$ plane for $m_\phi = 1$ GeV. The color captions are the same as in figure 9.

small λ_{Φ_ℓ} . In addition, by comparing the left and right plots in figure 8, one finds that $|\Delta a_\mu^{\Phi_\ell}|$ becomes smaller for smaller $\sin \delta_L$. Especially, in the case of $m_{\Phi_\ell} > 2$ TeV, $\lambda_{\Phi_\ell} < 0.1$ and $\sin \delta_L < 0.01$, we obtain $|\Delta a_\mu^{\Phi_\ell}| < 7.5 \times 10^{-13}$, which can be safely neglected. In the following, we will consider such a special case.

- The ϕ contribution Δa_μ^ϕ depends on the parameters $(\sin \delta_L, m_M, m_\phi, \lambda_\phi)$. We take $m_M = 300$ GeV as discussed in section 4.1, and show in figure 9 the 2σ allowed regions of (m_ϕ, λ_ϕ) for $\sin \delta_L = (1.0, 0.5, 0.1) \times 10^{-2}$. It can be seen that the ϕ boson can explain the $(g-2)_\mu$ anomaly at the 2σ level. Furthermore, larger λ_ϕ is required for larger m_ϕ and the lower limits on λ_ϕ depend only marginally on $\sin \delta_L$ for large m_ϕ . Taking $\lambda_\phi = 2$, we can then derive the 2σ allowed region of $(m_\phi, \sin \delta_L)$, which is shown in the left panel of figure 10. As can be seen from figures 9 and 10, smaller m_ϕ corresponds to a larger range of $\sin \delta_L$ and λ_ϕ . Hence, we take $m_\phi = 1$ GeV as a benchmark value and derive the allowed region of $(\lambda_\phi, \sin \delta_L)$, which is shown in the right panel of figure 10.
- The Z' contribution $\Delta a_\mu^{Z'}$ depends on the parameters $(m_{Z'}, m_M, g_\ell, \sin \delta_L)$ and is positive. However, different from the ϕ -boson case, the Z' can also affect the neutrino trident production. After considering the constraint from this rare process, the Z' contribution alone is not sufficient to explain the $(g-2)_\mu$ anomaly, as observed in the minimal $U(1)_{L_\mu-L_\tau}$ model [78].

As discussed above, in the case of $m_{\Phi_\ell} > 2$ TeV and $\lambda_{\Phi_\ell} < 0.1$, the relevant contributions to the $(g-2)_\mu$ arise from both the Z' and the ϕ boson. Thus, we consider them together, and

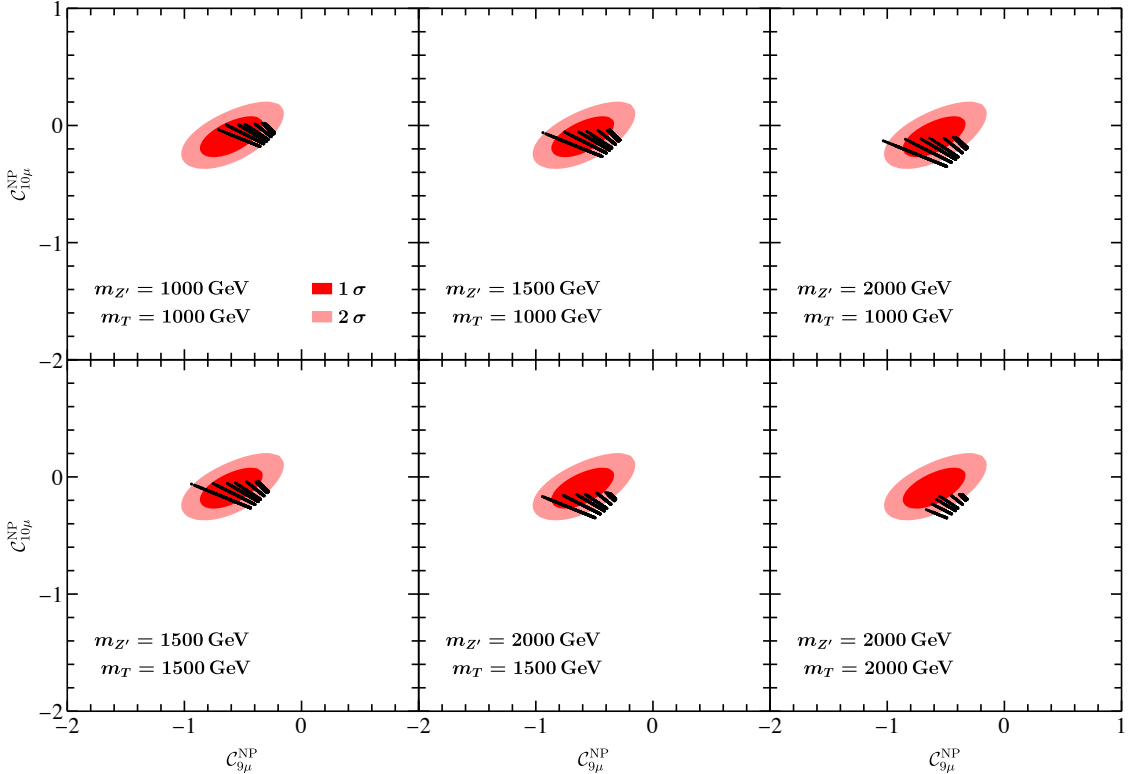


Figure 11: Constraints on $(\mathcal{C}_{9\mu}^{\text{NP}}, \mathcal{C}_{10\mu}^{\text{NP}})$ from a global fit of the $b \rightarrow s\ell^+\ell^-$ processes. The allowed regions at the 68% and the 95% confidence level (CL) are shown by the dark and the light red, respectively. The black points show the predicted values of $\mathcal{C}_{9\mu}^{\text{NP}}$ and $\mathcal{C}_{10\mu}^{\text{NP}}$ based on the whole allowed parameter space shown in figure 12.

take $m_M = 300$ GeV, $m_{Z'} = 1000$ GeV and $g_\ell = 2$ for simplicity. After taking into account the constraints from the $(g-2)_\mu$ anomaly and the neutrino trident production, we can derive the 2σ allowed regions of $(\sin\delta_L, m_\phi, \lambda_\phi)$, which are also shown in figures 9 and 10. One can see that the allowed regions become much larger compared to that obtained by including only the ϕ contribution. We take $m_\phi = 1$ GeV as a benchmark value, which approximately provides the largest parameter space for $\sin\delta_L$ and λ_ϕ , and show in figure 10 the allowed region of $(\lambda_\phi, \sin\delta_L)$. In this case, the lower bound on $\sin\delta_L$ is 3.2×10^{-4} and, after combining the bound derived in section 4.1, we obtain

$$3.2 \times 10^{-4} < \sin\delta_L < 1.0 \times 10^{-2}. \quad (4.4)$$

It is noted that the Z' and the ϕ contribution are both positive, and the latter alone can account for the $(g-2)_\mu$ anomaly while providing no influence on other processes discussed in section 3. Therefore, we will take $m_\phi = 1$ GeV and the bound in eq. (4.4) in the following analysis. This in turn implies that we do not need to consider the $(g-2)_\mu$ anomaly anymore when investigating the Z' contributions to other processes, as the anomaly can be definitely resolved in our model.

4.4 $b \rightarrow s\ell^+\ell^-$ processes

The most relevant observables to our model include the $b \rightarrow s\ell^+\ell^-$ transitions,³ the W -boson mass, the $(g-2)_\mu$, the neutrino trident production, as well as the $Z\mu\mu$ coupling. As discussed in the last

³The top partner can also affect the radiative $b \rightarrow s\gamma$ decays. However, the NP contribution is proportional to $\sin^2\theta_L$ and thus highly suppressed for small θ_L .

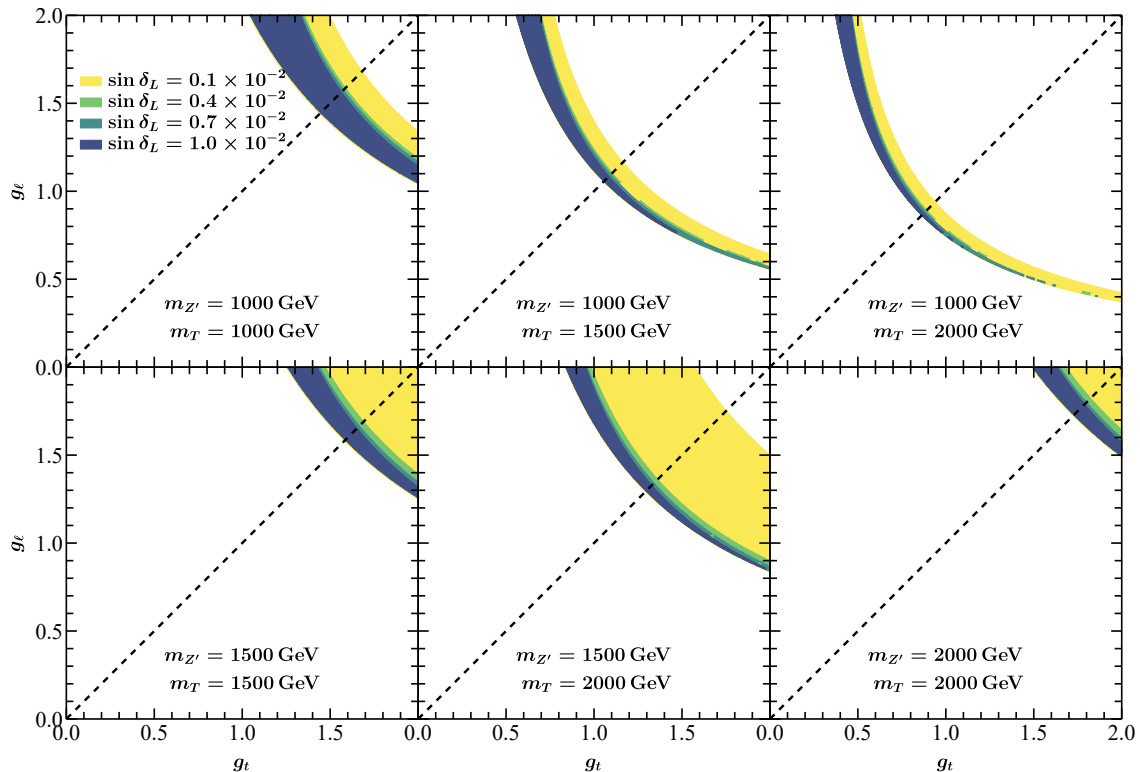


Figure 12: Constraints on $(\sin \theta_L, \sin \delta_L, g_t, g_\ell)$ for several benchmark values of $(m_{Z'}, m_T)$, plotted in the (g_t, g_ℓ) plane. The 2σ allowed regions for $\sin \delta_L = (0.1, 0.4, 0.7, 1.0) \times 10^{-2}$ are represented by different colors.

subsection, the ϕ contribution alone can explain the $(g-2)_\mu$ anomaly and, at the same time, does not bring any significant effect on other observables. Therefore, the remaining question is to see if the parameter space required to account for the latest CDF m_W measurement can also explain the $b \rightarrow s\ell^+\ell^-$ discrepancies, while satisfying the constraints from the neutrino trident production and the $Z\mu\mu$ coupling. This will be explored in this subsection.

For the $b \rightarrow s\ell^+\ell^-$ transitions, only the short-distance Wilson coefficients \mathcal{C}_9 and \mathcal{C}_{10} are affected in our model. Therefore, we will perform a global fit of $\mathcal{C}_{9\mu}^{\text{NP}}$ and $\mathcal{C}_{10\mu}^{\text{NP}}$ by considering the various measurements of the $b \rightarrow s\ell^+\ell^-$ processes, including the recent measurements of $R_{K^{(*)}}$ [14, 15] and $\mathcal{B}(B_s \rightarrow \mu^+\mu^-)$ [16]. Details of the fit are given in appendix B. The final allowed regions of $(\mathcal{C}_{9\mu}^{\text{NP}}, \mathcal{C}_{10\mu}^{\text{NP}})$ obtained through such a global fit are shown in figure 11, which are very similar to that of the latest global fits by other groups [23–27].

Since a small mixing angle θ_L is required to explain the latest CDF m_W measurement, the NP contributions to \mathcal{C}_9 and \mathcal{C}_{10} from the W -box, γ - and Z -penguin diagrams, which are all proportional to $\sin^2 \theta_L$, are highly suppressed. Therefore, the dominant contributions arise from the Z' -penguin diagrams, which depend on the parameters $(m_T, \sin \theta_L, m_M, \sin \delta_L, m_{Z'}, g_t, g_\ell)$. In the following, we take $m_M = 300$ GeV as discussed in section 4.1, and choose $(m_{Z'}, m_T) = (1.0, 1.0), (1.0, 1.5), (1.0, 2.0), (1.5, 1.5), (1.5, 2.0), (2.0, 2.0)$ TeV as several benchmark values. Then, the remaining relevant parameters are $(\sin \theta_L, \sin \delta_L, g_t, g_\ell)$. Considering the 2σ allowed regions obtained from the global EW fit as well as the constraints from the $b \rightarrow s\ell^+\ell^-$ global fit, the neutrino trident production and the $Z\mu\mu$ coupling,⁴ we can finally derive the allowed regions of these parameters.

⁴For the constraint from the $Z\mu\mu$ coupling, we take $\lambda_\phi = \lambda_{\Phi_\ell} = 1$, $m_\phi = 1$ GeV and $m_{\Phi_\ell} = 2$ TeV, as discussed

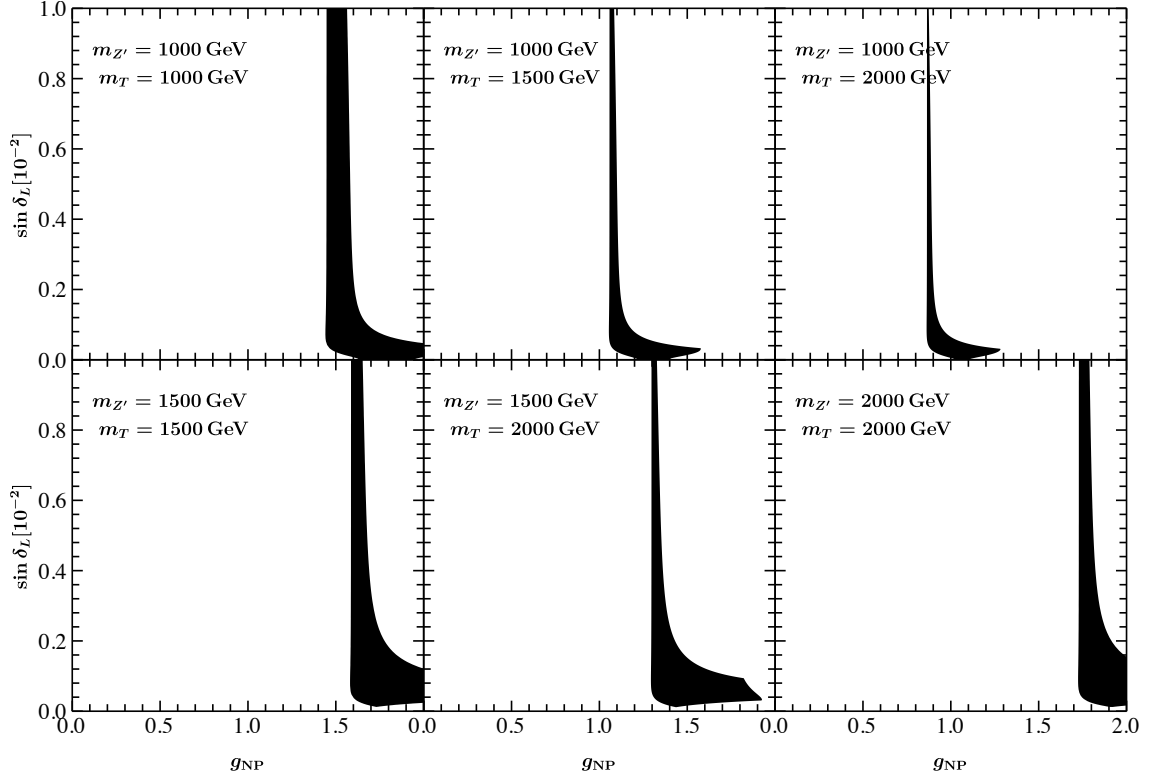


Figure 13: Constraints on the model parameters $(\sin \theta_L, \sin \delta_L, g_t, g_\ell)$ for several benchmark values of $(m_{Z'}, m_T)$ in the case of $g_t = g_\ell \equiv g_{\text{NP}}$, plotted in the $(g_{\text{NP}}, \sin \delta_L)$ plane. The 2σ allowed regions are shown in black.

As an illustration, we show in figure 12 the allowed regions in the (g_t, g_ℓ) plane for $\sin \delta_L = (0.1, 0.4, 0.7, 1.0) \times 10^{-2}$. It can be seen that the allowed values of the parameters g_t and g_ℓ for TeV-scale Z' and T are both of $\mathcal{O}(1)$ simultaneously, therefore being safely in the perturbative region. For heavier T or lighter Z' , smaller g_t and g_ℓ are required. In addition, for larger $\sin \delta_L$, the allowed regions of g_t and g_ℓ are reduced.

As a conclusion, our model can accommodate the $(g-2)_\mu$ anomaly, the latest CDF W -mass shift and the $b \rightarrow s\ell^+\ell^-$ discrepancies, while satisfying the other constraints like the neutrino trident production and the $Z \rightarrow \mu^+\mu^-$ processes. With the model parameters varied within the allowed regions, the predicted Wilson coefficients $\mathcal{C}_{9\mu}^{\text{NP}}$ and $\mathcal{C}_{10\mu}^{\text{NP}}$ are also shown in figure 11. From figure 12, we can also see that the departure of the ratio g_ℓ/g_t from unity is more stringently constrained for heavier Z' or lighter T . Furthermore, for different values of $(m_{Z'}, m_T)$, $g_t = g_\ell$ (or equivalently $g_\ell = g_t$) is always allowed. In the case of $g_t = g_\ell \equiv g_{\text{NP}}$, we show in figure 13 the allowed parameter space in the $(g_{\text{NP}}, \sin \delta_L)$ plane. Notably, this in turn implies that the possibility of $\Phi_t = \Phi_\ell^*$ is allowed in our model.⁵

4.5 Collider phenomenology

The vector-like top partner, being colored, can be efficiently produced at the hadron colliders [31, 92–94]. Searches for single and pair productions of the vector-like top partner have been performed at

in the section 4.1.

⁵The possibility of $\Phi_t = \Phi_\ell$ is, however, not possible, since $q_\ell = -q_t$ makes the sign of $\mathcal{C}_{9\mu}$ and $\mathcal{C}_{10\mu}$ (cf. eq. (3.15)) opposite to that shown in figure 11.

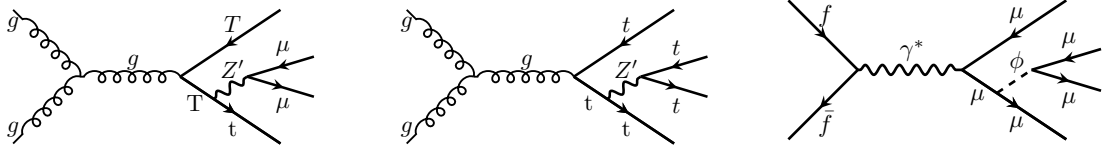


Figure 14: Representative Feynman diagrams for the processes $pp \rightarrow \mu^+ \mu^- + X$ (left), $pp \rightarrow t\bar{t}t\bar{t}$ (middle), and $pp(e^+e^-) \rightarrow \mu^+ \mu^- \mu^+ \mu^-$ (right) induced by the NP particles in our model.

the LHC, and strong constraints on its mass and mixing angle have been obtained [95–97]. However, in most of these searches, it is assumed that the top partner decays exclusively into the SM particles, *i.e.*, $T \rightarrow bW/tZ/th$, and the top partner has been excluded for masses below 1.3 TeV. In our model, this lower bound applies only for the case of $m_T < m_{Z'} + m_t$. In the case of $m_T > m_{Z'} + m_t$, on the other hand, the $T \rightarrow tZ'$ channel is open, and the bounds from these direct searches could be therefore relaxed [98–100]. In this case, as shown in figure 14, the cascade decay $T \rightarrow tZ' (\rightarrow \mu^+ \mu^-)$ makes the dimuon resonance searches at the LHC [101, 102] sensitive to our model. In order to derive the collider constraints, we take $m_\phi = 1$ GeV, $m_{\Phi_t} = m_{\Phi_\ell} = 2$ TeV and $m_M = 300$ GeV, and consider the allowed parameter space of $(\sin \theta_L, \sin \delta_L, g_t, g_\ell)$ derived in the last subsection, which corresponds to that shown in figure 12. For the dimuon resonance searches, the cross section is estimated by $\sigma(pp \rightarrow T\bar{T}) \cdot 2 \cdot \mathcal{B}(T \rightarrow tZ') \cdot \mathcal{B}(Z' \rightarrow \mu^+ \mu^-)$ and the result of $\sigma(pp \rightarrow T\bar{T})$ in ref. [95] is used. The total width of the top partner is calculated by considering all the tree-level two-body decay modes, which consist of $T \rightarrow tZ^{(\prime)}$, bW and th . Here the main decay channel is $T \rightarrow tZ'$ for small q_ℓ/q_t and $T \rightarrow th$ for large q_ℓ/q_t . For the Z' boson, its total width can be estimated by including all the tree-level two-body decay modes, which consist of $Z' \rightarrow M^+ M^-$, $M^+ \mu^-$, $\mu^+ M^-$, $\mu^+ \mu^-$, $\tau^+ \tau^-$, $\nu_\mu \bar{\nu}_\mu$, $\nu_\tau \bar{\nu}_\tau$ and $t\bar{t}$. The main decay channel is $Z' \rightarrow t\bar{t}$ for small q_ℓ/q_t . For large q_ℓ/q_t , on the other hand, the Z' decay is dominated by $Z' \rightarrow \tau^+ \tau^-$ and $Z' \rightarrow \nu_{\mu,\tau} \bar{\nu}_{\mu,\tau}$, while the branching ratio $\mathcal{B}(Z' \rightarrow \mu^+ \mu^-)$ can at most reach about 20%. The cross sections corresponding to the allowed parameter space can then be derived, which are shown as a function of q_ℓ/q_t in figure 15. It can be seen that the cross sections for various values of $m_{Z'}$ and m_T are all below the current CMS bound [102]. The cross section becomes larger for a lighter Z' ; especially for $m_T = 1.0$ TeV, the maximum cross section is close to the CMS bound. Furthermore, in most of the parameter space, the cross sections are higher than the sensitivities expected at the High-Luminosity LHC (HL-LHC) corresponding to 3000 fb^{-1} at $\sqrt{s} = 14$ TeV [105].

Searches for the multi-top final states [103, 106] can also provide evidence of the Z' boson [32]. As shown in figure 14, the Z' boson in this case can be produced in association with top pairs, and the decay $Z' \rightarrow t\bar{t}$ leads to the four-top final state $t\bar{t}t\bar{t}$. Similar to the analysis of the dimuon channel, we consider the allowed parameter space corresponding to figure 12. Predictions of the NP contributions to the $t\bar{t}t\bar{t}$ cross section are shown in figure 15, which are estimated by $\sigma_{\text{NP}}(pp \rightarrow t\bar{t}t\bar{t}) \approx \sigma(pp \rightarrow t\bar{t}Z') \cdot \mathcal{B}(Z' \rightarrow t\bar{t})$, with the result of $\sigma(pp \rightarrow t\bar{t}Z')$ taken from ref. [32]. It can be seen that our predictions for various values of $m_{Z'}$ and m_T are all well below the current CMS bound.⁶ Furthermore, the dimuon channel is enhanced by the NP contribution for large q_ℓ/q_t , while the four-top channel enhanced by small q_ℓ/q_t . Therefore, the two processes are complementary to each other in searching for the Z' boson.

Similar to the top partner, the vector-like lepton partner can also be pair-produced at the LHC. However, the production occurs only through the s channel involving the EW vector bosons, leading to much smaller cross sections [107, 108]. Searches for vector-like leptons have been performed at the LEP [109] and the LHC experiment [110, 111], and most of these studies focus on the case

⁶The recent ATLAS measurement [106] is roughly 1.8σ higher than the SM prediction [104]. For small g_ℓ/g_t , $\sigma(pp \rightarrow t\bar{t}t\bar{t})$ can be enhanced by $10 \sim 15\%$ compared to that in the SM. Thus, the tension is relaxed in our model.

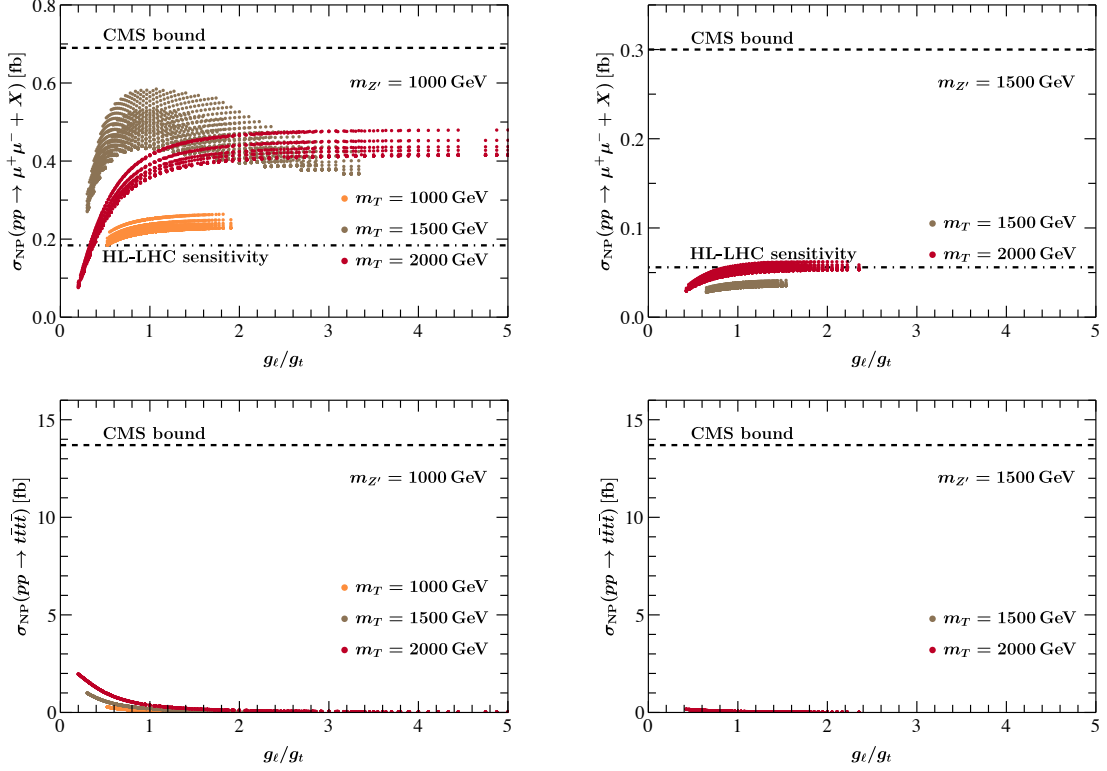


Figure 15: Predicted cross sections of the processes $pp \rightarrow \mu^+ \mu^- + X$ (top) and $pp \rightarrow t\bar{t}t\bar{t}$ (bottom), as well as the 95% CL upper bounds from the CMS experiment [102, 103]. For the $t\bar{t}t\bar{t}$ channel, the CMS upper bound is obtained by comparing the CMS measurement $17.7^{+3.7}_{-3.5}(\text{stat})^{+2.3}_{-1.9}(\text{syst})$ fb [103] with the SM prediction $13.4^{+1.0}_{-1.8}$ fb [104]. For the dimuon channel, the sensitivities expected at the HL-LHC corresponding to 3000 fb^{-1} at $\sqrt{s} = 14$ TeV [105] are also shown.

of vector-like tau partner. For example, by using 138 fb^{-1} of pp collisions at $\sqrt{s} = 13$ TeV, the $SU(2)_L$ doublet and singlet vector-like tau partner are already excluded for masses below 1045 GeV and in the mass range of 125 – 150 GeV, respectively [110]. In our model, due to the small mixing angle δ_L , the particle M can be approximated as a singlet vector-like muon partner. Similar to the case of the singlet vector-like tau partner, searches for the singlet vector-like muon partner is also very challenging for the LHC, due to its small production cross section. Based on the ATLAS searches for the anomalous productions of multi-lepton events [112], the vector-like muon partner has been investigated in ref. [113] (see ref. [114] for similar study by using the CMS data [115]). However, no limits on the vector-like muon partner are found for masses below 105 GeV or above 300 GeV. In addition, the LEP limit on additional heavy leptons [109] places a lower bound of around 100 GeV on the mass of the vector-like muon partner. Confronted with these experimental status, the benchmark value $m_M = 300$ GeV used in our numerical analysis is therefore reasonable. In addition, the muon partner lighter than around 300 GeV could produce a signal at the future proton-proton colliders [108]. Detailed analysis of the prospects for its discovery will be presented in a future work.

Besides the top partner, the muon partner and the Z' boson, signals of the scalars Φ_t , Φ_ℓ and ϕ can also be searched for at the high-energy colliders. For example, as shown in figure 14, the scalar ϕ can be produced in association with a muon pair, and the decay $\phi \rightarrow \mu^+ \mu^-$ leads to a four-muon final state, which has been measured at the LHC [116, 117] and the B factories [118, 119]. For

$m_\phi = 1 \text{ GeV}$, which has been used in our numerical analysis, future measurements at the Belle II [120] and the Super Tau-Charm Facility (STCF) [121] are expected to provide sensitive probes of this scalar. Detailed analysis of the current constraints on the scalars in our model and the future prospects at the LHC, Belle II and STCF is, however, beyond the scope of this paper, but will be explored in our future work.

5 Conclusion

In this paper, we have constructed a NP model that successfully addresses the latest CDF W -boson mass shift, the $(g-2)_\mu$ anomaly and the $b \rightarrow s\ell^+\ell^-$ discrepancies. In our setup, the SM is extended by the $SU(2)_L$ -singlet vector-like top and muon partners that are featured by additional $U(1)'$ gauge symmetry. The top and the muon partner have also the same SM quantum numbers as of the right-handed top and muon respectively, and can therefore mix with the latter after the EW and the $U(1)'$ symmetry breaking.

Similar to the SM case, the loop diagrams involving these fermion partners can contribute to the $(g-2)_\mu$, the W -boson mass m_W and the $b \rightarrow s\mu^+\mu^-$ transitions. After considering the most relevant constraints, such as the $Z \rightarrow \mu^+\mu^-$ decay and the neutrino trident production, both the $(g-2)_\mu$ anomaly and the latest CDF W -boson mass shift can be explained in our model. This requires that the mixing angles between the fermions and the fermion partners should be small. At the same time, the Z' -penguin diagrams involving the top partner can affect the short-distance Wilson coefficients $\mathcal{C}_{9\mu}$ and $\mathcal{C}_{10\mu}$ in the $b \rightarrow s\mu^+\mu^-$ transitions. Furthermore, the small lepton mixing angle δ_L makes the $Z'\mu\mu$ interaction almost of a vector-type. Therefore, $\mathcal{C}_{9\mu}^{\text{NP}} \ll \mathcal{C}_{10\mu}^{\text{NP}} \approx 0$ is obtained in our setup. This is also favored by the $b \rightarrow s\ell^+\ell^-$ global fit after including the recent measurements of $R_{K^{(*)}}$ [14, 15] and $\mathcal{B}(B_s \rightarrow \mu^+\mu^-)$ [16]. It is also found that both the Z' boson and the top partner can be as light as of $1 \sim 2 \text{ TeV}$, and thus may be accessible at the LHC Run 3 and its upgrade. Searches for the dimuon resonances and the top partner could also provide evidences of the Z' boson and the top partner. Especially, the Z' boson can enhance the $pp \rightarrow t\bar{t}t$ production cross section. Finally, the scalar ϕ with a mass of around 1 GeV can be produced in association with a muon pair, and the subsequent decay $\phi \rightarrow \mu^+\mu^-$ leads to a four-muon final state, which can be searched for at the Belle II and STCF experiments.

As a final comment, our model can be further explored in several phenomenological directions. By allowing for nonzero mixings of the top (muon) partner with the first and second (third) generations of quarks (leptons), several other interesting observables could be affected. In particular, the CKM matrix should be extended in this case, which may be responsible for the Cabibbo angle anomaly [122, 123]. Our model can also be extended by right-handed neutrinos or a dark sector. These points will be investigated in our future works.

Acknowledgments

This work is supported by the National Natural Science Foundation of China under Grant Nos. 12135006, 12075097 and 11805077, as well as by the Fundamental Research Funds for the Central Universities under Grant Nos. CCNU19TD012, CCNU20TS007 and CCNU22LJ004. XY is also supported in part by the Startup Research Funding from CCNU.

A One-loop corrections to $Z \rightarrow \ell^+\ell^-$

At the one-loop level, the NP contributions to the $Z \rightarrow \mu^+\mu^-$ decay arise from the diagrams shown in figure 5. In our calculation, the on-shell renormalization scheme specified in ref. [81] is adopted. Furthermore, in order to cancel the ultraviolet (UV) divergences, the renormalization of the mixing

with

$$\hat{C} = \begin{pmatrix} -\frac{1}{2}\hat{c}_L^2 + s_W^2 & -\frac{1}{2}\hat{s}_L\hat{c}_L \\ -\frac{1}{2}\hat{s}_L\hat{c}_L & -\frac{1}{2}\hat{s}_L^2 + s_W^2 \end{pmatrix}, \quad \hat{Z}_{L/R} = \begin{pmatrix} Z_{\mu\mu}^{L/R} & Z_{\mu M}^{L/R} \\ Z_{M\mu}^{L/R} & Z_{MM}^{L/R} \end{pmatrix}. \quad (\text{A.10})$$

In order to fix the renormalization of the mixing angle δ_L , we require the one-loop renormalized matrix element for the $Z \rightarrow \mu^+\mu^-$ decay is finite, *i.e.*,

$$\mathcal{M}(Z \rightarrow \mu^+\mu^-)|_{\text{UV}} = 0, \quad (\text{A.11})$$

By calculating the vertex-correction diagrams shown in figure 5, we find that this renormalization condition leads to the following renormalization constant:

$$\Delta\delta_L = -\frac{1}{2}\frac{\hat{c}_L}{\hat{s}_L}\delta Z_{\mu\mu}^L|_{\text{UV}} - \frac{1}{2}\delta Z_{\mu M}^L|_{\text{UV}}. \quad (\text{A.12})$$

It is also found that, with these prescriptions, the one-loop renormalized matrix elements for the decays $Z \rightarrow \ell_i^+\ell_j^-$ and $W^+ \rightarrow \ell_i^+\nu$ ($\ell_{i,j} = e$ or μ) are all finite after including the above renormalization constants.

B Global fit of $b \rightarrow s\ell^+\ell^-$ transitions

To perform a global fit of the $b \rightarrow s\ell^+\ell^-$ transitions, as done in refs. [126–129], we have considered the following experimental data: 1) the branching ratios of $B \rightarrow K\mu^+\mu^-$ [21], $B \rightarrow K^*\mu^+\mu^-$ [21, 130–132], $B_s \rightarrow \phi\mu^+\mu^-$ [22], $\Lambda_b \rightarrow \Lambda\mu^+\mu^-$ [133], $B \rightarrow X_s\mu^+\mu^-$ [134], and $B_s \rightarrow \mu^+\mu^-$ [16, 135]; 2) the angular distributions in $B \rightarrow K\mu^+\mu^-$ [130, 136], $B \rightarrow K^*\mu^+\mu^-$ [20, 131, 137–140], $B_s \rightarrow \phi\mu^+\mu^-$ [141], and $\Lambda_b \rightarrow \Lambda\mu^+\mu^-$ [142]; 3) the LFU ratios R_K and R_{K^*} [14, 15, 143–146].

During the global fit, we firstly construct a likelihood function that depends only on the short-distance Wilson coefficients \mathcal{C} [147],

$$-2\ln L(\mathcal{C}) = \mathbf{x}^T(\mathcal{C})[V_{\text{exp}} + V_{\text{th}}(\boldsymbol{\theta})]^{-1}\mathbf{x}(\mathcal{C}), \quad (\text{B.1})$$

where $\mathbf{x}_i(\mathcal{C}) = \mathcal{O}_i^{\text{fexp}} - \mathcal{O}_i^{\text{th}}(\mathcal{C}, \boldsymbol{\theta})$, with $\mathcal{O}_i^{\text{th}}$ and $\mathcal{O}_i^{\text{fexp}}$ representing the central values of the theoretical predictions and the experimental measurements, respectively. Their values depend on the input parameters $\boldsymbol{\theta}$ and the Wilson coefficients \mathcal{C} . Here V_{exp} and V_{th} denote the covariance matrices of the experimental measurements and the theoretical predictions, respectively. All the theoretical uncertainties and their correlations are included in V_{th} . Approximately, V_{th} can be obtained by fixing the Wilson coefficients \mathcal{C} to their default values within the SM. Furthermore, the theoretical uncertainties are approximated as Gaussian, which can be obtained by random samplings of the probability density functions of the input parameters $\boldsymbol{\theta}$. Finally, the $\Delta\chi^2$ function can be written as $\Delta\chi^2(\mathcal{C}) = -2\ln L(\mathcal{C})/L_{\text{max}}$, where L_{max} represents the maximum value of the likelihood function L for different values of the Wilson coefficients \mathcal{C} . More details about the fitting procedures can be found in refs. [147–149]. Here we have used an extended version of the package `flavio` [148] when performing such a global fit.

C Loop functions

Explicit expressions of the loop functions present in the oblique parameters S, T, U in eqs. (3.3)–(3.5) are listed below:

$$K_1(x, y) = -44x + 2\ln x + f_{-9}(x, x) - (x \rightarrow y), \quad (\text{C.1})$$

$$K_2(x, y) = (x - y)^2 - 3x - \left[(x - y)^3 - 3(x - y) - \frac{6xy}{x - y} \right] \ln x - f_3(x, x) + f_3(x, y) + (x \leftrightarrow y), \quad (\text{C.2})$$

$$K_3(x, y) = -3x - 6x^2 + (8 - 18x + 6x^3) \ln x - (12 - 18x + 6x^3) \ln(x - 1) - 32y + 4f_0(y, y), \quad (\text{C.3})$$

$$K_4(x, y) = -20x + 2 \ln x + f_{-3}(x, x) - (x \rightarrow y), \quad (\text{C.4})$$

$$K_5(x, y) = \frac{1}{x - y} \left[-3x^2 + 2x^3 - 6x^2y \right] - \left[(x - y)^3 + 3(x + y) + \frac{6x^2}{-x + y} \right] \ln x - f_3(x, x) + f_3(x, y) + (x \leftrightarrow y), \quad (\text{C.5})$$

$$K_6(x, y) = -x - 2x^2 + 2(2 - 3x + x^3) \ln \left[\frac{x}{x - 1} \right] - 16y + 2f_0(y, y), \quad (\text{C.6})$$

with the function $f_n(x, y)$ defined by

$$f_n(x, y) = -[(x + y - 1)^2 - 4xy - 3 + n(x + y)] \sqrt{4xy - (x + y - 1)^2} \cos^{-1} \left(\frac{x + y - 1}{\sqrt{4xy}} \right). \quad (\text{C.7})$$

Explicit expressions of the loop integrals I_{1-7} present in the short-distance Wilson coefficients $\mathcal{C}_9^{\text{NP}}$ and $\mathcal{C}_{10}^{\text{NP}}$ in section 3.2 are given, respectively, by

$$I_1 = f_t \left(-\frac{17}{6}, -\frac{7}{24}, \frac{1}{4} \right) + \left[-\frac{1}{4} + f_t \left(3, 3, \frac{1}{6}, -\frac{1}{4} \right) \right] \ln x_t - (t \rightarrow T), \quad (\text{C.8})$$

$$I_2 = \frac{3}{4} x_t - f_t \left(\frac{9}{4} \right) + \left[\frac{9}{4} + f_t \left(\frac{9}{2}, \frac{9}{4} \right) \right] \ln x_t - (t \rightarrow T), \quad (\text{C.9})$$

$$I_3 = 3(x_t + x_T) + \frac{3}{2} \frac{x_t x_T}{x_T - x_t} \ln \frac{x_t}{x_T}, \quad (\text{C.10})$$

$$I_4 = \frac{3x_t}{4} \left[\frac{1}{3} - f_t(1) + 2g(x_t, x_T) \ln x_t + (t \leftrightarrow T) \right], \quad (\text{C.11})$$

$$I_5 = \frac{x_t^2}{2} \left[\frac{1}{x_t} + \frac{2 \ln x_t}{x_T - x_t} + (t \leftrightarrow T) \right], \quad (\text{C.12})$$

$$I_6 = -\frac{(x_t - x_T)(x_t x_T - x_T - x_t + 4)}{2(x_t - 1)(x_T - 1)} - 3x_t^2 f_t(1) \ln x_t - (t \leftrightarrow T), \quad (\text{C.13})$$

$$I_7 = -(x_t + x_T) + 2 \frac{x_t x_T}{x_t - x_T} \ln \frac{x_t}{x_T}. \quad (\text{C.14})$$

where $x_t = m_t^2/m_W^2$, $x_T = m_T^2/m_W^2$, and the functions $g(x, y)$ and $f_q(a_1, a_2, a_3, \dots, a_n)$ are defined, respectively, as

$$g(x, y) = \frac{y(4 - 8y + y^2) + x(4 - 2y + y^2)}{6(x - y)(y - 1)^2}, \quad f_q(a_1, a_2, a_3, \dots, a_n) = \sum_{i=1}^n \frac{a_i}{(x_q - 1)^i}. \quad (\text{C.15})$$

The loop functions I_L and I_R introduced in eq. (3.31) are given, respectively, by

$$I_L = -(m_t^2 + m_T^2) + \frac{2m_t^2 m_T^2}{m_t^2 - m_T^2} \ln \frac{m_t^2}{m_T^2}, \quad I_R = 4m_T^2 - \frac{2(m_t^2 + m_T^2)m_T^2}{m_t^2 - m_T^2} \ln \frac{m_t^2}{m_T^2}. \quad (\text{C.16})$$

References

- [1] **Particle Data Group** Collaboration, R. L. Workman et al., *Review of Particle Physics, PTEP* **2022** (2022) 083C01. and 2023 update.

- [2] **Muon g-2** Collaboration, B. Abi et al., *Measurement of the Positive Muon Anomalous Magnetic Moment to 0.46 ppm*, *Phys. Rev. Lett.* **126** (2021), no. 14 141801, [[arXiv:2104.03281](#)].
- [3] **Muon g-2** Collaboration, G. W. Bennett et al., *Final Report of the Muon E821 Anomalous Magnetic Moment Measurement at BNL*, *Phys. Rev. D* **73** (2006) 072003, [[hep-ex/0602035](#)].
- [4] T. Aoyama et al., *The anomalous magnetic moment of the muon in the Standard Model*, *Phys. Rept.* **887** (2020) 1–166, [[arXiv:2006.04822](#)].
- [5] S. Borsanyi et al., *Leading hadronic contribution to the muon magnetic moment from lattice QCD*, *Nature* **593** (2021), no. 7857 51–55, [[arXiv:2002.12347](#)].
- [6] M. C e et al., *Window observable for the hadronic vacuum polarization contribution to the muon g-2 from lattice QCD*, *Phys. Rev. D* **106** (2022), no. 11 114502, [[arXiv:2206.06582](#)].
- [7] **Extended Twisted Mass** Collaboration, C. Alexandrou et al., *Lattice calculation of the short and intermediate time-distance hadronic vacuum polarization contributions to the muon magnetic moment using twisted-mass fermions*, *Phys. Rev. D* **107** (2023), no. 7 074506, [[arXiv:2206.15084](#)].
- [8] T. Blum et al., *An update of Euclidean windows of the hadronic vacuum polarization*, [arXiv:2301.08696](#).
- [9] **CMD-3** Collaboration, F. V. Ignatov et al., *Measurement of the $e^+e^- \rightarrow \pi^+\pi^-$ cross section from threshold to 1.2 GeV with the CMD-3 detector*, [arXiv:2302.08834](#).
- [10] G. Colangelo et al., *Prospects for precise predictions of a_μ in the Standard Model*, [arXiv:2203.15810](#).
- [11] **CDF** Collaboration, T. Aaltonen et al., *High-precision measurement of the W boson mass with the CDF II detector*, *Science* **376** (2022), no. 6589 170–176.
- [12] **LHCb** Collaboration, R. Aaij et al., *Measurement of the W boson mass*, *JHEP* **01** (2022) 036, [[arXiv:2109.01113](#)].
- [13] **ATLAS** Collaboration, *Improved W boson Mass Measurement using 7 TeV Proton-Proton Collisions with the ATLAS Detector*, .
- [14] **LHCb** Collaboration, *Test of lepton universality in $b \rightarrow s\ell^+\ell^-$ decays*, [arXiv:2212.09152](#).
- [15] **LHCb** Collaboration, *Measurement of lepton universality parameters in $B^+ \rightarrow K^+\ell^+\ell^-$ and $B^0 \rightarrow K^{*0}\ell^+\ell^-$ decays*, [arXiv:2212.09153](#).
- [16] **CMS** Collaboration, *Measurement of the $B_S^0 \rightarrow \mu^+\mu^-$ decay properties and search for the $B^0 \rightarrow \mu^+\mu^-$ decay in proton-proton collisions at $\sqrt{s} = 13$ TeV*, [arXiv:2212.10311](#).
- [17] **Heavy Flavor Averaging Group, HFLAV** Collaboration, Y. S. Amhis et al., *Averages of b-hadron, c-hadron, and τ -lepton properties as of 2021*, *Phys. Rev. D* **107** (2023), no. 5 052008, [[arXiv:2206.07501](#)]. and online updates.
- [18] C. Bobeth, M. Gorbahn, T. Hermann, M. Misiak, E. Stamou, and M. Steinhauser, *$B_{s,d} \rightarrow l^+l^-$ in the Standard Model with Reduced Theoretical Uncertainty*, *Phys. Rev. Lett.* **112** (2014) 101801, [[arXiv:1311.0903](#)].
- [19] M. Beneke, C. Bobeth, and R. Szafron, *Enhanced electromagnetic correction to the rare B-meson decay $B_{s,d} \rightarrow \mu^+\mu^-$* , *Phys. Rev. Lett.* **120** (2018), no. 1 011801, [[arXiv:1708.09152](#)].
- [20] **LHCb** Collaboration, R. Aaij et al., *Measurement of CP-Averaged Observables in the $B^0 \rightarrow K^{*0}\mu^+\mu^-$ Decay*, *Phys. Rev. Lett.* **125** (2020), no. 1 011802, [[arXiv:2003.04831](#)].
- [21] **LHCb** Collaboration, R. Aaij et al., *Differential branching fractions and isospin asymmetries of $B \rightarrow K^{(*)}\mu^+\mu^-$ decays*, *JHEP* **06** (2014) 133, [[arXiv:1403.8044](#)].
- [22] **LHCb** Collaboration, R. Aaij et al., *Branching Fraction Measurements of the Rare $B_s^0 \rightarrow \phi\mu^+\mu^-$ and $B_s^0 \rightarrow f_2'(1525)\mu^+\mu^-$ Decays*, *Phys. Rev. Lett.* **127** (2021), no. 15 151801, [[arXiv:2105.14007](#)].

- [23] N. Gubernari, M. Reboud, D. van Dyk, and J. Virto, *Improved theory predictions and global analysis of exclusive $b \rightarrow s\mu^+\mu^-$ processes*, *JHEP* **09** (2022) 133, [[arXiv:2206.03797](#)].
- [24] A. Greljo, J. Salko, A. Smolkovič, and P. Stangl, *Rare b decays meet high-mass Drell-Yan*, *JHEP* **05** (2023) 087, [[arXiv:2212.10497](#)].
- [25] M. Ciuchini, M. Fedele, E. Franco, A. Paul, L. Silvestrini, and M. Valli, *Constraints on lepton universality violation from rare B decays*, *Phys. Rev. D* **107** (2023), no. 5 055036, [[arXiv:2212.10516](#)].
- [26] M. Algueró, A. Biswas, B. Capdevila, S. Descotes-Genon, J. Matias, and M. Novoa-Brunet, *To (b)e or not to (b)e: No electrons at LHCb*, [arXiv:2304.07330](#).
- [27] Q. Wen and F. Xu, *The Global Fits of New Physics in $b \rightarrow s$ after $R_{K^{(*)}}$ 2022 Release*, [arXiv:2305.19038](#).
- [28] X.-Q. Li, Z.-J. Xie, Y.-D. Yang, and X.-B. Yuan, *Correlating the CDF W -boson mass shift with the $b \rightarrow s\ell^+\ell^-$ anomalies*, *Phys. Lett. B* **838** (2023) 137651, [[arXiv:2205.02205](#)].
- [29] J. F. Kamenik, Y. Soreq, and J. Zupan, *Lepton flavor universality violation without new sources of quark flavor violation*, *Phys. Rev. D* **97** (2018), no. 3 035002, [[arXiv:1704.06005](#)].
- [30] S. Fajfer, A. Greljo, J. F. Kamenik, and I. Mustac, *Light Higgs and Vector-like Quarks without Prejudice*, *JHEP* **07** (2013) 155, [[arXiv:1304.4219](#)].
- [31] J. A. Aguilar-Saavedra, *Mixing with vector-like quarks: constraints and expectations*, *EPJ Web Conf.* **60** (2013) 16012, [[arXiv:1306.4432](#)].
- [32] P. J. Fox, I. Low, and Y. Zhang, *Top-philic Z' forces at the LHC*, *JHEP* **03** (2018) 074, [[arXiv:1801.03505](#)].
- [33] F. del Aguila and M. J. Bowick, *The Possibility of New Fermions With $\Delta I = 0$ Mass*, *Nucl. Phys. B* **224** (1983) 107.
- [34] G. C. Branco and L. Lavoura, *On the Addition of Vector Like Quarks to the Standard Model*, *Nucl. Phys. B* **278** (1986) 738–754.
- [35] P. Langacker and D. London, *Mixing Between Ordinary and Exotic Fermions*, *Phys. Rev. D* **38** (1988) 886.
- [36] L. Lavoura and J. P. Silva, *The Oblique corrections from vector - like singlet and doublet quarks*, *Phys. Rev. D* **47** (1993) 2046–2057.
- [37] F. del Aguila, M. Perez-Victoria, and J. Santiago, *Observable contributions of new exotic quarks to quark mixing*, *JHEP* **09** (2000) 011, [[hep-ph/0007316](#)].
- [38] Y. Okada and L. Panizzi, *LHC signatures of vector-like quarks*, *Adv. High Energy Phys.* **2013** (2013) 364936, [[arXiv:1207.5607](#)].
- [39] S. Dawson and E. Furlan, *A Higgs Conundrum with Vector Fermions*, *Phys. Rev. D* **86** (2012) 015021, [[arXiv:1205.4733](#)].
- [40] J. A. Aguilar-Saavedra, R. Benbrik, S. Heinemeyer, and M. Pérez-Victoria, *Handbook of vectorlike quarks: Mixing and single production*, *Phys. Rev. D* **88** (2013), no. 9 094010, [[arXiv:1306.0572](#)].
- [41] S. A. R. Ellis, R. M. Godbole, S. Gopalakrishna, and J. D. Wells, *Survey of vector-like fermion extensions of the Standard Model and their phenomenological implications*, *JHEP* **09** (2014) 130, [[arXiv:1404.4398](#)].
- [42] J. a. M. Alves, G. C. Branco, A. L. Cherchiglia, C. C. Nishi, J. T. Penedo, P. M. F. Pereira, M. N. Rebelo, and J. I. Silva-Marcos, *Vector-like Singlet Quarks: a Roadmap*, [arXiv:2304.10561](#).
- [43] X. G. He, G. C. Joshi, H. Lew, and R. R. Volkas, *NEW Z -prime PHENOMENOLOGY*, *Phys. Rev. D* **43** (1991) 22–24.

- [44] X.-G. He, G. C. Joshi, H. Lew, and R. R. Volkas, *Simplest Z-prime model*, *Phys. Rev. D* **44** (1991) 2118–2132.
- [45] A. Alloul, N. D. Christensen, C. Degrande, C. Duhr, and B. Fuks, *FeynRules 2.0 - A complete toolbox for tree-level phenomenology*, *Comput. Phys. Commun.* **185** (2014) 2250–2300, [[arXiv:1310.1921](#)].
- [46] T. Hahn, *Generating Feynman diagrams and amplitudes with FeynArts 3*, *Comput. Phys. Commun.* **140** (2001) 418–431, [[hep-ph/0012260](#)].
- [47] R. Mertig, M. Bohm, and A. Denner, *FEYN CALC: Computer algebraic calculation of Feynman amplitudes*, *Comput. Phys. Commun.* **64** (1991) 345–359.
- [48] V. Shtabovenko, R. Mertig, and F. Orellana, *New Developments in FeynCalc 9.0*, *Comput. Phys. Commun.* **207** (2016) 432–444, [[arXiv:1601.01167](#)].
- [49] V. Shtabovenko, R. Mertig, and F. Orellana, *FeynCalc 9.3: New features and improvements*, *Comput. Phys. Commun.* **256** (2020) 107478, [[arXiv:2001.04407](#)].
- [50] H. H. Patel, *Package-X 2.0: A Mathematica package for the analytic calculation of one-loop integrals*, *Comput. Phys. Commun.* **218** (2017) 66–70, [[arXiv:1612.00009](#)].
- [51] W. F. L. Hollik, *Radiative Corrections in the Standard Model and their Role for Precision Tests of the Electroweak Theory*, *Fortsch. Phys.* **38** (1990) 165–260.
- [52] P. Langacker, M.-x. Luo, and A. K. Mann, *High precision electroweak experiments: A Global search for new physics beyond the standard model*, *Rev. Mod. Phys.* **64** (1992) 87–192.
- [53] J. Erler and M. Schott, *Electroweak Precision Tests of the Standard Model after the Discovery of the Higgs Boson*, *Prog. Part. Nucl. Phys.* **106** (2019) 68–119, [[arXiv:1902.05142](#)].
- [54] H. Flacher, M. Goebel, J. Haller, A. Hocker, K. Monig, and J. Stelzer, *Revisiting the Global Electroweak Fit of the Standard Model and Beyond with Gfitter*, *Eur. Phys. J. C* **60** (2009) 543–583, [[arXiv:0811.0009](#)]. [Erratum: *Eur.Phys.J.C* 71, 1718 (2011)].
- [55] **Gfitter Group** Collaboration, M. Baak, J. Cúth, J. Haller, A. Hoecker, R. Kogler, K. Mönig, M. Schott, and J. Stelzer, *The global electroweak fit at NNLO and prospects for the LHC and ILC*, *Eur. Phys. J. C* **74** (2014) 3046, [[arXiv:1407.3792](#)].
- [56] J. Haller, A. Hoecker, R. Kogler, K. Mönig, T. Peiffer, and J. Stelzer, *Update of the global electroweak fit and constraints on two-Higgs-doublet models*, *Eur. Phys. J. C* **78** (2018), no. 8 675, [[arXiv:1803.01853](#)].
- [57] J. de Blas, M. Ciuchini, E. Franco, A. Goncalves, S. Mishima, M. Pierini, L. Reina, and L. Silvestrini, *Global analysis of electroweak data in the Standard Model*, *Phys. Rev. D* **106** (2022), no. 3 033003, [[arXiv:2112.07274](#)].
- [58] R. Balkin, E. Madge, T. Menzo, G. Perez, Y. Soreq, and J. Zupan, *On the implications of positive W mass shift*, *JHEP* **05** (2022) 133, [[arXiv:2204.05992](#)].
- [59] M. Endo and S. Mishima, *New physics interpretation of W-boson mass anomaly*, *Phys. Rev. D* **106** (2022), no. 11 115005, [[arXiv:2204.05965](#)].
- [60] K. S. Babu, S. Jana, and V. P. K., *Correlating W-Boson Mass Shift with Muon $g-2$ in the Two Higgs Doublet Model*, *Phys. Rev. Lett.* **129** (2022), no. 12 121803, [[arXiv:2204.05303](#)].
- [61] A. Strumia, *Interpreting electroweak precision data including the W-mass CDF anomaly*, *JHEP* **08** (2022) 248, [[arXiv:2204.04191](#)].
- [62] P. Asadi, C. Cesarotti, K. Fraser, S. Homiller, and A. Parikh, *Oblique Lessons from the W Mass Measurement at CDF II*, [[arXiv:2204.05283](#)].
- [63] J. Gu, Z. Liu, T. Ma, and J. Shu, *Speculations on the W-mass measurement at CDF**, *Chin. Phys. C* **46** (2022), no. 12 123107, [[arXiv:2204.05296](#)].

- [64] C.-T. Lu, L. Wu, Y. Wu, and B. Zhu, *Electroweak precision fit and new physics in light of the W boson mass*, *Phys. Rev. D* **106** (2022), no. 3 035034, [[arXiv:2204.03796](#)].
- [65] J. de Blas, M. Pierini, L. Reina, and L. Silvestrini, *Impact of the Recent Measurements of the Top-Quark and W -Boson Masses on Electroweak Precision Fits*, *Phys. Rev. Lett.* **129** (2022), no. 27 271801, [[arXiv:2204.04204](#)].
- [66] M. E. Peskin and T. Takeuchi, *Estimation of oblique electroweak corrections*, *Phys. Rev. D* **46** (1992) 381–409.
- [67] M. E. Peskin and T. Takeuchi, *A New constraint on a strongly interacting Higgs sector*, *Phys. Rev. Lett.* **65** (1990) 964–967.
- [68] I. Maksymyk, C. P. Burgess, and D. London, *Beyond S , T and U* , *Phys. Rev. D* **50** (1994) 529–535, [[hep-ph/9306267](#)].
- [69] F. Domingo and T. Lenz, *W mass and Leptonic Z -decays in the NMSSM*, *JHEP* **07** (2011) 101, [[arXiv:1101.4758](#)].
- [70] S. Heinemeyer, W. Hollik, D. Stockinger, A. M. Weber, and G. Weiglein, *Precise prediction for $M(W)$ in the MSSM*, *JHEP* **08** (2006) 052, [[hep-ph/0604147](#)].
- [71] M. Awramik, M. Czakon, A. Freitas, and G. Weiglein, *Precise prediction for the W boson mass in the standard model*, *Phys. Rev. D* **69** (2004) 053006, [[hep-ph/0311148](#)].
- [72] G. Buchalla, A. J. Buras, and M. E. Lautenbacher, *Weak decays beyond leading logarithms*, *Rev. Mod. Phys.* **68** (1996) 1125–1144, [[hep-ph/9512380](#)].
- [73] F. Jegerlehner and A. Nyffeler, *The Muon $g-2$* , *Phys. Rept.* **477** (2009) 1–110, [[arXiv:0902.3360](#)].
- [74] **CHARM-II** Collaboration, D. Geiregat et al., *First observation of neutrino trident production*, *Phys. Lett. B* **245** (1990) 271–275.
- [75] **CCFR** Collaboration, S. R. Mishra et al., *Neutrino tridents and WZ interference*, *Phys. Rev. Lett.* **66** (1991) 3117–3120.
- [76] **NuTeV** Collaboration, T. Adams et al., *Neutrino trident production from NuTeV*, in *29th International Conference on High-Energy Physics*, pp. 631–634, 7, 1998. [[hep-ex/9811012](#)].
- [77] **NuTeV** Collaboration, T. Adams et al., *Evidence for diffractive charm production in muon-neutrino Fe and anti-muon-neutrino Fe scattering at the Tevatron*, *Phys. Rev. D* **61** (2000) 092001, [[hep-ex/9909041](#)].
- [78] W. Altmannshofer, S. Gori, M. Pospelov, and I. Yavin, *Neutrino Trident Production: A Powerful Probe of New Physics with Neutrino Beams*, *Phys. Rev. Lett.* **113** (2014) 091801, [[arXiv:1406.2332](#)].
- [79] W. Altmannshofer, S. Gori, M. Pospelov, and I. Yavin, *Quark flavor transitions in $L_\mu - L_\tau$ models*, *Phys. Rev. D* **89** (2014) 095033, [[arXiv:1403.1269](#)].
- [80] **ALEPH, DELPHI, L3, OPAL, SLD, LEP Electroweak Working Group, SLD Electroweak Group, SLD Heavy Flavour Group** Collaboration, S. Schael et al., *Precision electroweak measurements on the Z resonance*, *Phys. Rept.* **427** (2006) 257–454, [[hep-ex/0509008](#)].
- [81] A. Denner, *Techniques for calculation of electroweak radiative corrections at the one loop level and results for W physics at LEP-200*, *Fortsch. Phys.* **41** (1993) 307–420, [[arXiv:0709.1075](#)].
- [82] J. E. Camargo-Molina, A. Celis, and D. A. Faroughy, *Anomalies in Bottom from new physics in Top*, *Phys. Lett. B* **784** (2018) 284–293, [[arXiv:1805.04917](#)].
- [83] B. A. Dobrescu and F. Yu, *Dijet and electroweak limits on a Z' boson coupled to quarks*, [[arXiv:2112.05392](#)].
- [84] P. Arnan, D. Becirevic, F. Mescia, and O. Sumensari, *Probing low energy scalar leptoquarks by the leptonic W and Z couplings*, *JHEP* **02** (2019) 109, [[arXiv:1901.06315](#)].

- [85] **Flavour Lattice Averaging Group (FLAG) Collaboration**, Y. Aoki et al., *FLAG Review 2021*, *Eur. Phys. J. C* **82** (2022), no. 10 869, [[arXiv:2111.09849](#)].
- [86] **CKMfitter Group Collaboration**, J. Charles, A. Hocker, H. Lacker, S. Laplace, F. R. Le Diberder, J. Malcles, J. Ocariz, M. Pivk, and L. Roos, *CP violation and the CKM matrix: Assessing the impact of the asymmetric B factories*, *Eur. Phys. J. C* **41** (2005), no. 1 1–131, [[hep-ph/0406184](#)]. updated results and plots available at: <http://ckmfitter.in2p3.fr>.
- [87] G. Altarelli, T. Sjostrand, and F. Zwirner, eds., *Physics at LEP2: Vol. 1*, CERN Yellow Reports: Conference Proceedings, 2, 1996.
- [88] J. De Blas et al., *HEPfit: a code for the combination of indirect and direct constraints on high energy physics models*, *Eur. Phys. J. C* **80** (2020), no. 5 456, [[arXiv:1910.14012](#)].
- [89] P. J. Fox, J. Liu, D. Tucker-Smith, and N. Weiner, *An Effective Z'*, *Phys. Rev. D* **84** (2011) 115006, [[arXiv:1104.4127](#)].
- [90] **CMS Collaboration**, A. M. Sirunyan et al., *Combined measurements of Higgs boson couplings in proton–proton collisions at $\sqrt{s} = 13$ TeV*, *Eur. Phys. J. C* **79** (2019), no. 5 421, [[arXiv:1809.10733](#)].
- [91] **ATLAS Collaboration**, *A combination of measurements of Higgs boson production and decay using up to 139 fb^{-1} of proton–proton collision data at $\sqrt{s} = 13$ TeV collected with the ATLAS experiment*, .
- [92] N. Greiner, K. Kong, J.-C. Park, S. C. Park, and J.-C. Winter, *Model-Independent Production of a Top-Philic Resonance at the LHC*, *JHEP* **04** (2015) 029, [[arXiv:1410.6099](#)].
- [93] P. Cox, A. D. Medina, T. S. Ray, and A. Spray, *Novel collider and dark matter phenomenology of a top-philic Z'*, *JHEP* **06** (2016) 110, [[arXiv:1512.00471](#)].
- [94] J. H. Kim, K. Kong, S. J. Lee, and G. Mohlabeng, *Probing TeV scale Top-Philic Resonances with Boosted Top-Tagging at the High Luminosity LHC*, *Phys. Rev. D* **94** (2016), no. 3 035023, [[arXiv:1604.07421](#)].
- [95] **ATLAS Collaboration**, M. Aaboud et al., *Combination of the searches for pair-produced vector-like partners of the third-generation quarks at $\sqrt{s} = 13$ TeV with the ATLAS detector*, *Phys. Rev. Lett.* **121** (2018), no. 21 211801, [[arXiv:1808.02343](#)].
- [96] **CMS Collaboration**, A. Tumasyan et al., *Search for single production of a vector-like T quark decaying to a top quark and a Z boson in the final state with jets and missing transverse momentum at $\sqrt{s} = 13$ TeV*, *JHEP* **05** (2022) 093, [[arXiv:2201.02227](#)].
- [97] H. de la TorreTrisha Farooque and T. Farooque, *Looking beyond the Standard Model with Third Generation Quarks at the LHC*, *Symmetry* **14** (2022), no. 3 444.
- [98] J. Serra, *Beyond the Minimal Top Partner Decay*, *JHEP* **09** (2015) 176, [[arXiv:1506.05110](#)].
- [99] A. Anandakrishnan, J. H. Collins, M. Farina, E. Kuflik, and M. Perelstein, *Odd Top Partners at the LHC*, *Phys. Rev. D* **93** (2016), no. 7 075009, [[arXiv:1506.05130](#)].
- [100] N. Bizot, G. Cacciapaglia, and T. Flacke, *Common exotic decays of top partners*, *JHEP* **06** (2018) 065, [[arXiv:1803.00021](#)].
- [101] **ATLAS Collaboration**, G. Aad et al., *Search for high-mass dilepton resonances using 139 fb^{-1} of pp collision data collected at $\sqrt{s} = 13$ TeV with the ATLAS detector*, *Phys. Lett. B* **796** (2019) 68–87, [[arXiv:1903.06248](#)].
- [102] **CMS Collaboration**, A. M. Sirunyan et al., *Search for resonant and nonresonant new phenomena in high-mass dilepton final states at $\sqrt{s} = 13$ TeV*, *JHEP* **07** (2021) 208, [[arXiv:2103.02708](#)].
- [103] **CMS Collaboration**, A. Hayrapetyan et al., *Observation of four top quark production in proton–proton collisions at $\sqrt{s} = 13$ TeV*, [arXiv:2305.13439](#).

- [104] M. van Beekveld, A. Kulesza, and L. M. Valero, *Threshold resummation for the production of four top quarks at the LHC*, [arXiv:2212.03259](#).
- [105] **CMS** Collaboration, *Sensitivity projections for a search for new phenomena at high dilepton mass for the LHC Run 3 and the HL-LHC*, .
- [106] **ATLAS** Collaboration, G. Aad et al., *Observation of four-top-quark production in the multilepton final state with the ATLAS detector*, [arXiv:2303.15061](#).
- [107] N. Kumar and S. P. Martin, *Vectorlike Leptons at the Large Hadron Collider*, *Phys. Rev. D* **92** (2015), no. 11 115018, [[arXiv:1510.03456](#)].
- [108] P. N. Bhattiprolu and S. P. Martin, *Prospects for vectorlike leptons at future proton-proton colliders*, *Phys. Rev. D* **100** (2019), no. 1 015033, [[arXiv:1905.00498](#)].
- [109] **L3** Collaboration, P. Achard et al., *Search for heavy neutral and charged leptons in e^+e^- annihilation at LEP*, *Phys. Lett. B* **517** (2001) 75–85, [[hep-ex/0107015](#)].
- [110] **CMS** Collaboration, A. Tumasyan et al., *Inclusive nonresonant multilepton probes of new phenomena at $\sqrt{s}=13$ TeV*, *Phys. Rev. D* **105** (2022), no. 11 112007, [[arXiv:2202.08676](#)].
- [111] **ATLAS** Collaboration, *Search for third-generation vector-like leptons in pp collisions at $\sqrt{s} = 13$ TeV with the ATLAS detector*, [arXiv:2303.05441](#).
- [112] **ATLAS** Collaboration, *Search for New Physics in Events with Three Charged Leptons with the ATLAS detector*, .
- [113] R. Dermisek, J. P. Hall, E. Lunghi, and S. Shin, *Limits on Vectorlike Leptons from Searches for Anomalous Production of Multi-Lepton Events*, *JHEP* **12** (2014) 013, [[arXiv:1408.3123](#)].
- [114] A. Falkowski, D. M. Straub, and A. Vicente, *Vector-like leptons: Higgs decays and collider phenomenology*, *JHEP* **05** (2014) 092, [[arXiv:1312.5329](#)].
- [115] **CMS** Collaboration, *A search for anomalous production of events with three or more leptons using 19.5/fb of $\sqrt{s}=8$ TeV LHC data*, .
- [116] **CMS** Collaboration, A. M. Sirunyan et al., *Search for an $L_\mu - L_\tau$ gauge boson using $Z \rightarrow 4\mu$ events in proton-proton collisions at $\sqrt{s} = 13$ TeV*, *Phys. Lett. B* **792** (2019) 345–368, [[arXiv:1808.03684](#)].
- [117] **ATLAS** Collaboration, *Search for a new Z' gauge boson in 4μ events with the ATLAS experiment*, [arXiv:2301.09342](#).
- [118] **BaBar** Collaboration, J. P. Lees et al., *Search for a muonic dark force at BABAR*, *Phys. Rev. D* **94** (2016), no. 1 011102, [[arXiv:1606.03501](#)].
- [119] **Belle** Collaboration, T. Czank et al., *Search for $Z' \rightarrow \mu + \mu^-$ in the $L_\mu - L_\tau$ gauge-symmetric model at Belle*, *Phys. Rev. D* **106** (2022), no. 1 012003, [[arXiv:2109.08596](#)].
- [120] **Belle II** Collaboration, M. Laurenza, *Dark-sector physics at Belle II*, *PoS PANIC2021* (2022) 047.
- [121] M. Achasov et al., *STCF Conceptual Design Report: Volume I - Physics & Detector*, [arXiv:2303.15790](#).
- [122] B. Belfatto and Z. Berezhiani, *Are the CKM anomalies induced by vector-like quarks? Limits from flavor changing and Standard Model precision tests*, *JHEP* **10** (2021) 079, [[arXiv:2103.05549](#)].
- [123] A. Crivellin, M. Kirk, T. Kitahara, and F. Mescia, *Global fit of modified quark couplings to EW gauge bosons and vector-like quarks in light of the Cabibbo angle anomaly*, *JHEP* **03** (2023) 234, [[arXiv:2212.06862](#)].
- [124] A. Denner, S. Dittmaier, and J.-N. Lang, *Renormalization of mixing angles*, *JHEP* **11** (2018) 104, [[arXiv:1808.03466](#)].
- [125] S. Kanemura, Y. Okada, E. Senaha, and C. P. Yuan, *Higgs coupling constants as a probe of new physics*, *Phys. Rev. D* **70** (2004) 115002, [[hep-ph/0408364](#)].

- [126] W. Altmannshofer, C. Niehoff, P. Stangl, and D. M. Straub, *Status of the $B \rightarrow K^* \mu^+ \mu^-$ anomaly after Moriond 2017*, *Eur. Phys. J. C* **77** (2017), no. 6 377, [[arXiv:1703.09189](#)].
- [127] W. Altmannshofer, P. Stangl, and D. M. Straub, *Interpreting Hints for Lepton Flavor Universality Violation*, *Phys. Rev. D* **96** (2017), no. 5 055008, [[arXiv:1704.05435](#)].
- [128] J. Aebischer, W. Altmannshofer, D. Guadagnoli, M. Reboud, P. Stangl, and D. M. Straub, *B-decay discrepancies after Moriond 2019*, *Eur. Phys. J. C* **80** (2020), no. 3 252, [[arXiv:1903.10434](#)].
- [129] W. Altmannshofer and P. Stangl, *New physics in rare B decays after Moriond 2021*, *Eur. Phys. J. C* **81** (2021), no. 10 952, [[arXiv:2103.13370](#)].
- [130] **CDF** Collaboration, *Precise Measurements of Exclusive $b \rightarrow s\mu^+\mu^-$ Decay Amplitudes Using the Full CDF Data Set*, .
- [131] **CMS** Collaboration, V. Khachatryan et al., *Angular analysis of the decay $B^0 \rightarrow K^{*0} \mu^+ \mu^-$ from pp collisions at $\sqrt{s} = 8$ TeV*, *Phys. Lett. B* **753** (2016) 424–448, [[arXiv:1507.08126](#)].
- [132] **LHCb** Collaboration, R. Aaij et al., *Measurements of the S-wave fraction in $B^0 \rightarrow K^+ \pi^- \mu^+ \mu^-$ decays and the $B^0 \rightarrow K^*(892)^0 \mu^+ \mu^-$ differential branching fraction*, *JHEP* **11** (2016) 047, [[arXiv:1606.04731](#)]. [Erratum: JHEP 04, 142 (2017)].
- [133] **LHCb** Collaboration, R. Aaij et al., *Differential branching fraction and angular analysis of $\Lambda_b^0 \rightarrow \Lambda \mu^+ \mu^-$ decays*, *JHEP* **06** (2015) 115, [[arXiv:1503.07138](#)]. [Erratum: JHEP 09, 145 (2018)].
- [134] **BaBar** Collaboration, J. P. Lees et al., *Measurement of the $B \rightarrow X_s l^+ l^-$ branching fraction and search for direct CP violation from a sum of exclusive final states*, *Phys. Rev. Lett.* **112** (2014) 211802, [[arXiv:1312.5364](#)].
- [135] **LHCb** Collaboration, R. Aaij et al., *Analysis of Neutral B-Meson Decays into Two Muons*, *Phys. Rev. Lett.* **128** (2022), no. 4 041801, [[arXiv:2108.09284](#)].
- [136] **LHCb** Collaboration, R. Aaij et al., *Angular analysis of charged and neutral $B \rightarrow K \mu^+ \mu^-$ decays*, *JHEP* **05** (2014) 082, [[arXiv:1403.8045](#)].
- [137] **Belle** Collaboration, S. Wehle et al., *Lepton-Flavor-Dependent Angular Analysis of $B \rightarrow K^* \ell^+ \ell^-$* , *Phys. Rev. Lett.* **118** (2017), no. 11 111801, [[arXiv:1612.05014](#)].
- [138] **CMS** Collaboration, *Measurement of the P_1 and P'_5 angular parameters of the decay $B^0 \rightarrow K^{*0} \mu^+ \mu^-$ in proton-proton collisions at $\sqrt{s} = 8$ TeV*, .
- [139] **ATLAS** Collaboration, M. Aaboud et al., *Angular analysis of $B_d^0 \rightarrow K^* \mu^+ \mu^-$ decays in pp collisions at $\sqrt{s} = 8$ TeV with the ATLAS detector*, *JHEP* **10** (2018) 047, [[arXiv:1805.04000](#)].
- [140] **LHCb** Collaboration, R. Aaij et al., *Angular Analysis of the $B^+ \rightarrow K^{*+} \mu^+ \mu^-$ Decay*, *Phys. Rev. Lett.* **126** (2021), no. 16 161802, [[arXiv:2012.13241](#)].
- [141] **LHCb** Collaboration, R. Aaij et al., *Angular analysis of the rare decay $B_s^0 \rightarrow \phi \mu^+ \mu^-$* , *JHEP* **11** (2021) 043, [[arXiv:2107.13428](#)].
- [142] **LHCb** Collaboration, R. Aaij et al., *Angular moments of the decay $\Lambda_b^0 \rightarrow \Lambda \mu^+ \mu^-$ at low hadronic recoil*, *JHEP* **09** (2018) 146, [[arXiv:1808.00264](#)].
- [143] **BaBar** Collaboration, J. P. Lees et al., *Measurement of Branching Fractions and Rate Asymmetries in the Rare Decays $B \rightarrow K^{(*)} l^+ l^-$* , *Phys. Rev. D* **86** (2012) 032012, [[arXiv:1204.3933](#)].
- [144] **Belle** Collaboration, A. Abdesselam et al., *Test of Lepton-Flavor Universality in $B \rightarrow K^* \ell^+ \ell^-$ Decays at Belle*, *Phys. Rev. Lett.* **126** (2021), no. 16 161801, [[arXiv:1904.02440](#)].
- [145] **BELLE** Collaboration, S. Choudhury et al., *Test of lepton flavor universality and search for lepton flavor violation in $B \rightarrow K \ell \ell$ decays*, *JHEP* **03** (2021) 105, [[arXiv:1908.01848](#)].
- [146] **LHCb** Collaboration, R. Aaij et al., *Tests of lepton universality using $B^0 \rightarrow K_S^0 \ell^+ \ell^-$ and $B^+ \rightarrow K^{*+} \ell^+ \ell^-$ decays*, *Phys. Rev. Lett.* **128** (2022), no. 19 191802, [[arXiv:2110.09501](#)].

- [147] W. Altmannshofer and D. M. Straub, *New physics in $b \rightarrow s$ transitions after LHC run 1*, *Eur. Phys. J. C* **75** (2015), no. 8 382, [[arXiv:1411.3161](#)].
- [148] D. M. Straub, *flavio: a Python package for flavour and precision phenomenology in the Standard Model and beyond*, [[arXiv:1810.08132](#)].
- [149] X.-Q. Li, M. Shen, D.-Y. Wang, Y.-D. Yang, and X.-B. Yuan, *Explaining the $b \rightarrow s\ell^+\ell^-$ anomalies in Z' scenarios with top-FCNC couplings*, *Nucl. Phys. B* **980** (2022) 115828, [[arXiv:2112.14215](#)].
- [150] L.-S. Geng, B. Grinstein, S. Jäger, S.-Y. Li, J. Martin Camalich, and R.-X. Shi, *Implications of new evidence for lepton-universality violation in $b \rightarrow s\ell^+\ell^-$ decays*, *Phys. Rev. D* **104** (2021), no. 3 035029, [[arXiv:2103.12738](#)].
- [151] C. Cornella, D. A. Faroughy, J. Fuentes-Martin, G. Isidori, and M. Neubert, *Reading the footprints of the B -meson flavor anomalies*, *JHEP* **08** (2021) 050, [[arXiv:2103.16558](#)].
- [152] M. Algueró, B. Capdevila, S. Descotes-Genon, J. Matias, and M. Novoa-Brunet, *$b \rightarrow s\ell^+\ell^-$ global fits after R_{K_S} and $R_{K^{*+}}$* , *Eur. Phys. J. C* **82** (2022), no. 4 326, [[arXiv:2104.08921](#)].
- [153] T. Hurth, F. Mahmoudi, D. M. Santos, and S. Neshatpour, *More Indications for Lepton Nonuniversality in $b \rightarrow s\ell^+\ell^-$* , *Phys. Lett. B* **824** (2022) 136838, [[arXiv:2104.10058](#)].
- [154] J. Aebischer, J. Kumar, P. Stangl, and D. M. Straub, *A Global Likelihood for Precision Constraints and Flavour Anomalies*, *Eur. Phys. J. C* **79** (2019), no. 6 509, [[arXiv:1810.07698](#)].
- [155] B. Allanach and J. Davighi, *M_W helps select Z' models for $b \rightarrow s\ell\ell$ anomalies*, *Eur. Phys. J. C* **82** (2022), no. 8 745, [[arXiv:2205.12252](#)].